

Development of a Specific and Potent IGF2BP1 Inhibitor: A Promising Therapeutic Agent for IGF2BP1-expressing Cancers

Amandeep Singh^{a1}, Vikash Singh^{c1}, Nadav Wallis^{b1}, Giancarlo Abis^{d,e}, Froma Oberman^b, Tyler Wood^c, Mayura Dhamdhere^c, Tehila Gershon^b, Andres Ramos^d, Joel Yisraeli^b, Vladimir S. Spiegelman^{c*}, and Arun K. Sharma^{a*}

^aThe Pennsylvania State University College of Medicine, Department of Pharmacology, Penn State Cancer Institute, Hershey, PA, USA

^bDepartment of Developmental Biology and Cancer Research, Institute for Medical Research – Israel-Canada, Hebrew University Hadassah Medical School, Jerusalem, Israel

^c Division of Pediatric Hematology and Oncology, Department of Pediatrics, The Pennsylvania State University College of Medicine, Hershey, PA, USA.

^d Division of Biosciences, Institute of Structural and Molecular Biology, University College London, Darwin Building, Gower Street, London WC1E 6BT, United Kingdom

^e Current address: Randall Centre for Cell & Molecular Biophysics, King's College London, New Hunt's House, Newcomen Street, SE1 1UL

¹ These authors have contributed equally

* Authors to whom correspondence should be addressed

Arun K. Sharma, Ph.D.
Department of Pharmacology
Penn State Cancer Institute, CH72
Penn State College of Medicine
500 University Drive
Hershey, PA 17033
Phone: 717-531-4563
Fax: 717-531-0244
E-mail: aks14@psu.edu

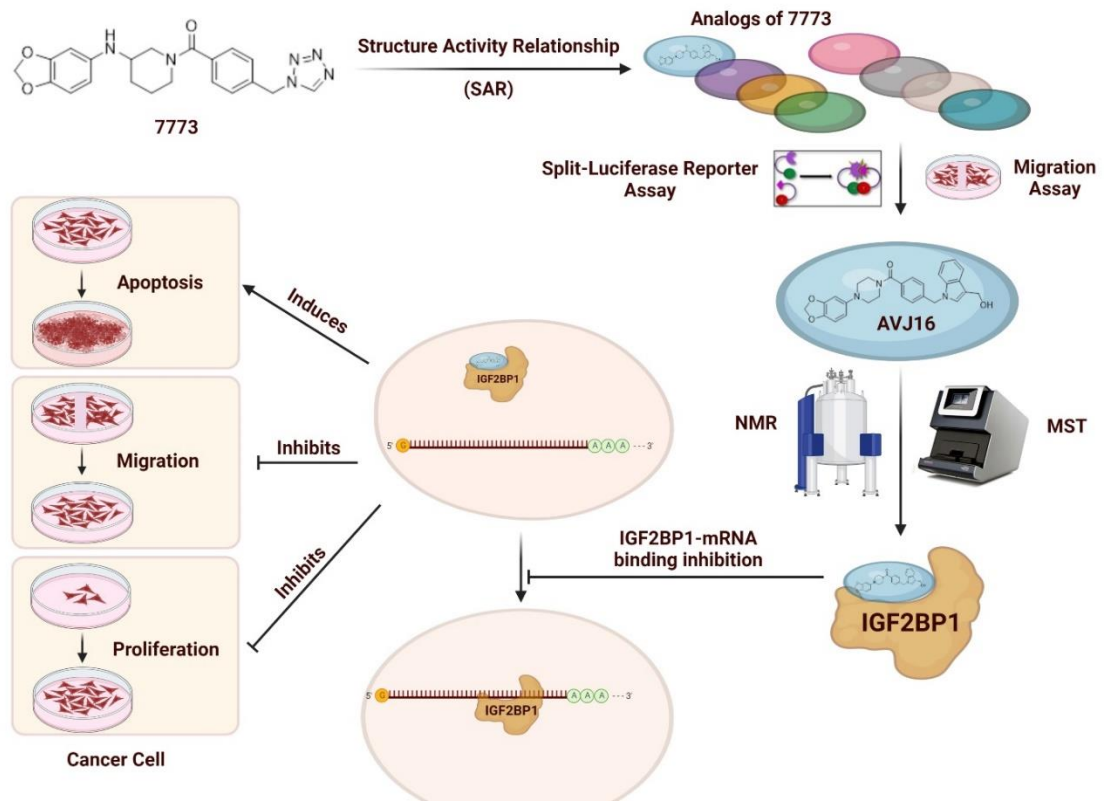
Or

Vladimir S. Spiegelman, MD, PhD
Department of Pediatrics
Division of Pediatric Hematology/Oncology
PO Box 850, MC H085, C7833E
500 University Drive
Hershey, Pennsylvania 17033-0850
Ph: 717-531-6719
FAX: 717-531-4789
E-mail: vspiegelman@pennstatehealth.psu.edu

Highlights

- Optimization of **7773** ~~led to the identification of~~revealed six compounds that performed ~~equally well~~similar or better than **7773**.
- **AVJ16** was found to be most efficient at preventing cell migration.
- ~~The direct binding of~~**AVJ16** showed a 12-fold increase in binding efficiency to IGF2BP1 ~~was validated by binding tests, with as~~ 12-fold increase in binding efficiency over ~~compared to~~ **7773**~~the lead compound~~.
- **AVJ16** ~~was shown to binds~~ to a hydrophobic region at the protein's KH34 di-domain interface ~~between the KH3 and KH4 domains~~.

Graphical Abstract



Abstract

IGF2BP1 is a protein that controls the stability, localization, and translation of various mRNA targets. Poor clinical outcomes in numerous cancer types have been associated with its overexpression. As it has been demonstrated to impede tumor growth and metastasis in animal models, inhibiting IGF2BP1 function is a promising strategy for combating cancer. A lead chemical, **7773**, which specifically decreased IGF2BP1 RNA binding and cellular activities, was identified in a high-throughput screen for effective IGF2BP1 inhibitors. Additional optimization led to the discovery of six compounds that performed equally well or better than **7773**. In cell lines with high levels of endogenous IGF2BP1, one of **7773** derivatives, **AVJ16**, was found to be most efficient at preventing cell migration. Further, **AVJ16** was found to be IGF2BP1-specific because it had no effect on cell lines that expressed little or no IGF2BP1 protein. The direct binding of **AVJ16** to IGF2BP1 was validated by binding tests, with a 12-fold increase in binding efficiency over the lead compound. **AVJ16** was shown to bind to a hydrophobic region at the protein's KH34 di-domain interface between the KH3 and KH4 domains. Overall, the findings imply that **AVJ16** is a potent and specific inhibitor of IGF2BP1 activity.

Keywords: IGF2BP1, High-throughput Screen, Structure-Activity Relationship, Wound Healing, ¹⁵N-HSQC

1. Introduction

Insulin-like growth factor 2 mRNA binding protein 1 (IGF2BP1) is an RNA-binding protein with six RNA binding domains that control its target mRNAs' translation, localization, stability, and alternative splicing.[1] IGF2BP1 is expressed ubiquitously during embryonic development, but its expression in adult tissue is minimal.[2] High levels of IGF2BP1 expression are associated with poor prognosis in patients with various malignancies, including melanoma, neuroblastoma, hepatocellular carcinoma, squamous cell carcinoma, and lung, ovarian, breast, and colorectal cancers (CRC).[3-7] mRNAs of numerous tumor-promoting genes, including c-Myc, β TrCP1, GLI1, MITF, KRAS, and MDR1, are among the targets of IGF2BP1.[8-12] It exerts its influence by interacting with specific mRNA targets, often those encoding key proteins involved in cell cycle regulation, apoptosis evasion, and epithelial-mesenchymal transition. Through these interactions, IGF2BP1 contributes to the rewiring of cellular processes that are essential for cancer cell survival and dissemination.[13] Because IGF2BP1 is expressed during development, turned off after birth, and then activated upon carcinogenesis, it has been referred to as an "oncofetal" factor. In addition, inhibition or knockdown of IGF2BP1 sensitizes malignant cells to chemotherapeutic drugs and targeted therapy.[14-18]

Importantly, the intestinal-specific knockout of IGF2BP1 was shown to drastically reduce the number of intestinal tumors in *ApcMin/+* mouse model of intestinal tumorigenesis.[19] The most common cause of mortality in cancer patients is metastasis, and IGF2BP1 was shown to be involved in melanoma and lung adenocarcinoma (LUAD) metastasis.[20, 21] There is an urgent need to develop effective metastasis-specific therapeutic agents to treat cancer patients, and IGF2BP1's pleiotropic effect on multiple pro-tumorigenic and pro-metastatic pathways makes it an attractive target.[22]

Despite the fact that many RNA-binding proteins (RBPs) have been established as promising therapeutic targets, most RBPs are regarded as "undruggable"; due to a lack of well-defined binding sites. Targeting RBPs with small molecules is therefore not trivial. IGF2BP1 is a member of the IGF2 mRNA-binding protein family, characterized by its distinctive RNA recognition motifs (RRMs) and K-homology (KH) domains. These structural motifs allow IGF2BP1 to bind to specific RNA sequences within target mRNAs, enabling it to regulate their stability, translation, and localization. The multi-domain architecture of IGF2BP1 endows it with the ability to

recognize and bind to a diverse array of target mRNAs, contributing to its role in various cellular processes.[23] The KH3-KH4 di-domain plays a predominant role in IGF2BP1 RNA-binding, including its recognition of m6A methylation of the corresponding RNA sequences, although in some cases all four KH domains of IGF2BP1 are required [24-28]. Inhibiting an RBP's RNA binding activity by blocking its interaction with target RNA is one way of interfering with its intended role.[29] Thus, our previous study carried out a high throughput screen of over 27,000 small compounds using fluorescence polarization (FP) to identify effective IGF2BP1 inhibitors.[30] In various in vitro and cell-based experiments, the most promising candidates were further validated. These tests led us to discover the compound **7773** that was highly specific in blocking IGF2BP1 RNA binding and a number of its biological functions. Here, we have carried out a structure-activity relationship (SAR) analysis to improve the **7773** lead compound further. These experiments have generated more selective and efficient small-molecule inhibitors of IGF2BP1, one of which, **AVJ16**, represents a strong candidate for further development as an anti-cancer drug.

2. Results

2.1. Design: To optimize the lead compound **7773** and create more selective, effective, and safe small-molecule inhibitors of IGF2BP1 that could be developed clinically as cancer therapeutics, we conducted an SAR study based on **7773** analogs. Twenty-five novel compounds were designed and synthesized by altering/substituting rings A, B, and C of the parent lead molecule (Figure 1). Basic skeleton and overall length of the structure of new molecules was maintained similar to the lead compound so as to preserve the active site binding while enhancing the binding potential. Three different series of compounds were synthesized. Series 1 involved modification of ring C using several 5- and 6-membered heterocycles and open chain thiourea and selenocyanate functionalities (Scheme 1). Series 2 involved replacement of piperidine ring B by a piperazine ring along with changes in ring C. Series 3 included modification of ring A along with changes in rings B and C. SAR studies identified compound **13g** (**AVJ16**), having an indole-3-carbinol (I3C) moiety (ring C) and piperazine as the connecting ring B, as the most selective and potent inhibitor of IGF2BP1. I3C is a naturally occurring compound shown to possess anti-cancer activity in several preclinical models. It has been reported to suppress the proliferation of various cancer cell

lines, including breast, colon, prostate, and endometrium, at a concentration of 50–100 μM . [31, 32]

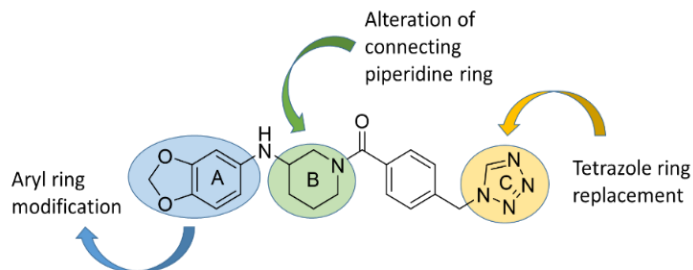
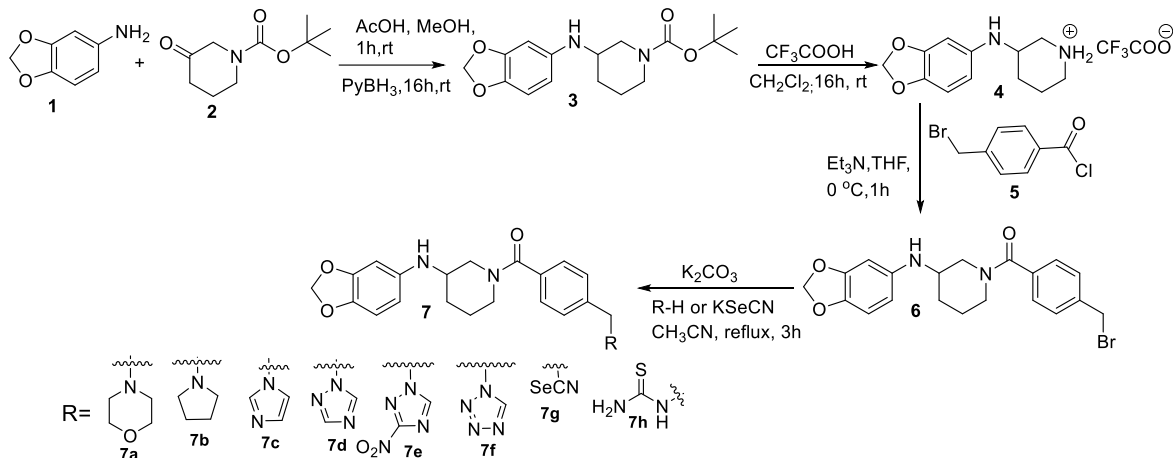


Figure 1. Structure of the lead compound **7773** and its sites of structural optimization.

2.2. CHEMISTRY

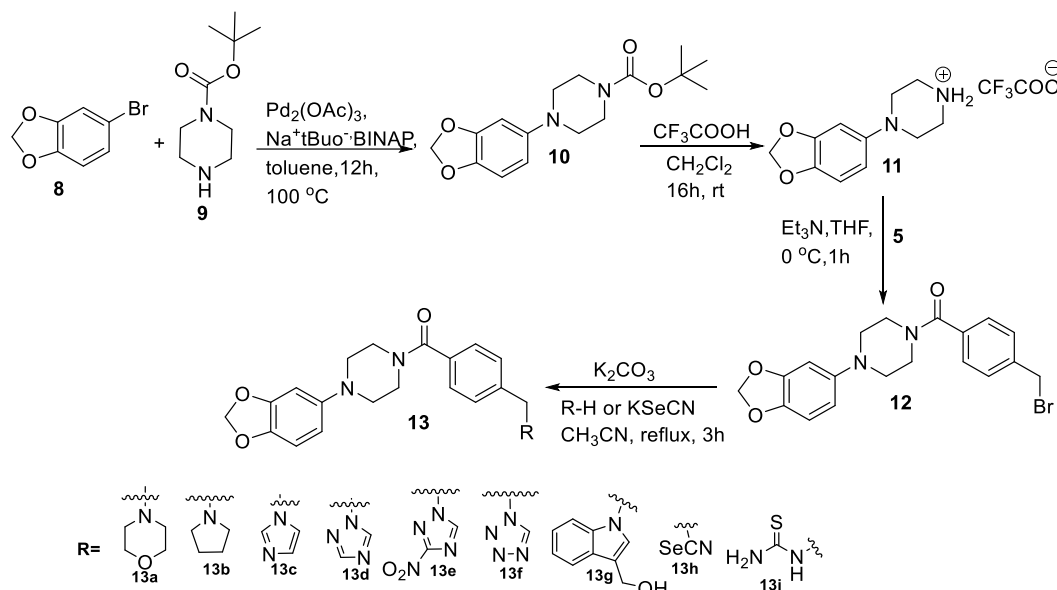
The synthesis of '7773' analogs **7a-h** is outlined in Scheme 1. Treatment of 4-amino-1,2-(methylenedioxy)benzene (**1**) with *N*-*boc*-protected piperadone **2** in the presence of acetic acid and pyridine complex of BH_3 in dry methanol yielded intermediate **3**. Deprotection of **3** with trifluoroacetic acid afforded intermediate **4** which on subsequent treatment with 4-(bromomethyl)benzoyl chloride (**5**) produced precursor **6**. Reaction of **6** with various heterocycles in the presence of base, potassium selenocyanate and thiourea yielded desired compounds **7a-h**. The structures of the compounds were assigned based on NMR spectroscopy and high-resolution mass spectrometry (HRMS). For example, compound **7c** showed a molecular ion peak at 404.1848 in its mass spectrum. Its ^1H NMR spectrum showed the presence of a multiplet at δ 1.46-1.50 corresponding to 2H (- CH_2 of piperidine) along with two singlets at δ 5.23 (2H) of methylene and at δ 5.91 (2H) corresponding to dioxy-1,2-methylene group. The presence of characteristic three singlets at δ 6.93 (1H) and δ 7.15 (1H) and δ 7.72 (1H) of imidazole ring protons confirmed the assigned structure. The appearance of peaks at δ 29.5, 31.1, 49.7, 49.8, and 65.2 due to piperidine ring carbons along with the presence of a resonance at δ 169.5 due to amide carbonyl in ^{13}C NMR spectrum further corroborated the assigned structure.

Scheme 1: Synthesis of analogs 7a-h



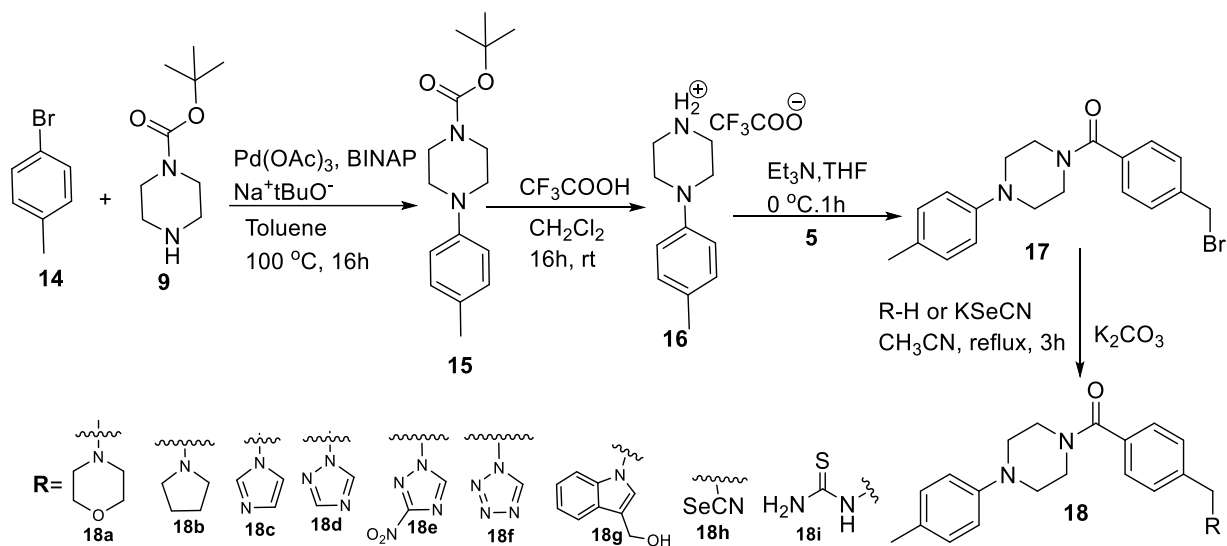
Synthesis of analogs **13a-i** (Scheme 2) involved palladium catalyzed Buchwald–Hartwig reaction between 3,4-(methylenedioxy)aniline (**8**) and Boc-protected piperazine **9** in the presence of sodium tert-butoxide as a base to yield intermediate **10**. Deprotection of **10** with trifluoroacetic acid yielded compound **11** which upon reaction with 4-(bromomethyl)benzoyl chloride (**5**) resulted in the formation of precursor **12**. Treatment of various heterocycles with **12** in the presence of potassium carbonate as a base yielded desired analogs **13a-i** in good yields (Scheme 2). The structures of the synthesized analogs were assigned based on spectral studies and analytical evidence. The compound **13g** (**AVJ16**), for example, exhibited a molecular ion peak at 469.2002 in its HRMS. Its ^1H NMR spectrum showed the presence of a doublet at δ 4.65 corresponding to 2H (O-CH₂ of indole) along with singlets at δ 4.43 (2H) of methylene groups. The appearance of a singlet at δ 5.91 (2H) corresponding to dioxy-1,2-methylene group along with a characteristic pair of two doublets at δ 7.26 (2H) and 7.36 (2H) because of *para*-substituted benzene ring protons confirmed the assigned structure. The appearance of peaks at δ 42.3, 47.7, and 51.6 due to piperazine ring carbons along with the presence of peak at δ 169.1 due to amide carbonyl in ^{13}C NMR spectrum further corroborated the assigned structure.

Scheme 2: Synthesis of analogs **13a-i**



The syntheses of analogs **18a-i** followed a similar series of reactions as adapted for compounds **13**, starting with 4-bromotoluene as depicted in Scheme 3. The desired precursor **17** was synthesized starting with Pd catalyzed Buchwald–Hartwig coupling between 4-bromotoluene and *N*-Boc protected piperazine in the presence of toluene as a solvent to afford intermediate **15**, which was deprotected with the help of trifluoroacetic acid to yield *p*-tolyl-piperazine **16**, followed by further reaction of **16** with 4-(bromomethyl)benzoyl chloride (**5**) in the presence of triethylamine and dry THF. Potassium carbonate promoted reaction between precursor **17** and various heterocycles yielded the desired analogs **18a-i** which were purified by flash chromatography using a mixture of 3:7 (MeOH:CH₂Cl₂) as an eluent. The structures of the compounds were assigned on the basis of spectroscopy techniques and analytical evidence. For example, compound **18h** exhibited a molecular ion peak at 362.1855 in its HRMS. Its ¹H NMR spectrum showed the presence of a singlet at δ 2.20 corresponding to 3H (methyl group) along with singlet at δ 6.03 (2H) due to the presence of –CH₂ protons of the methylene group. The appearance of two doublets at δ 6.85 (2H) and at 7.04 (2H) confirmed the presence of para-substituted benzene ring protons along with a characteristic singlet at δ 9.02 (1H) corresponding to the tetrazole ring proton. The appearance of peaks at δ 41.9, 47.4, and 49.4 in the ¹³C NMR spectrum of **18h** corresponding to piperazine ring carbons and the presence of an amide carbonyl carbon at δ 168.9 further supported the assigned structure.

Scheme 3: Synthesis of analogs **18a-i**



2.3. BIOLOGY

2.3.1. Structure-Activity Relationship

To examine the structure–activity relationship, all synthesized compounds were first evaluated for IGF2BP1 inhibition utilizing our previously-described cell-based split-luciferase reporter assay with compound **7773** serving as reference (Figure 2).[30] The activity profiles of all the compounds ranged from moderate to good. The activity of the compounds having piperidine as A ring depended upon the nature of moieties as C ring (**7a-h**). Compounds with morpholine (**7a**) and pyrrolidine (**7b**) used as ring C showed comparable activity to **7773**. Replacement of ring C with imidazole (**7c**) and triazole (**7d**) moieties did not improve the efficacy of the compounds. The introduction of an electron-withdrawing nitro group on triazole ring (**7e**) increased the activity profile and showed enhanced efficacy compared to standard compound **7f** (**7773**). Compound **7g** having selenocyanate group, and **7h** having thiourea functionality as an open chain moiety, also showed improved activity profiles. To explore the structure–activity relationship, piperidine ring was replaced by piperazine ring and new series of compounds (**13a-i**) were synthesized. It is evident from Figure 2 that compounds having morpholine (**13a**) and pyrrolidine (**13b**) moieties as a C ring, were more active as compared to compounds **7a** and **7b**. Replacement of ring C with imidazole (**13c**), triazole (**13d**), nitro triazole (**13e**) and tetrazole (**13f**) groups resulted in loss of

activity. However, compound having I3C moiety (**13g**) as a ring C was found to be more active. The introduction of thiourea (**13i**) group instead of cyclic ring in compound **13** also improved the activity profile. However, replacing thiourea with selenocyanate (**13h**) reduced the activity. Interestingly, the series of compounds (**18a-i**) synthesized by replacing the ring A with a *p*-tolyl moiety were inactive as compared to compounds having benzo-1,3-dioxole as a ring A, except compounds (**18e**) and (**18g**) having nitroimidazole and I3C as ring C. To rule out the possible effect of compounds on enzymatic activity of luciferase itself we have tested selected compounds for their effect on control (not split-) luciferase. Supplemental figure 1S shows that compound showing most activity in multiple assays (**13g**, **AVJ16**) had no effect on control luciferase activity.

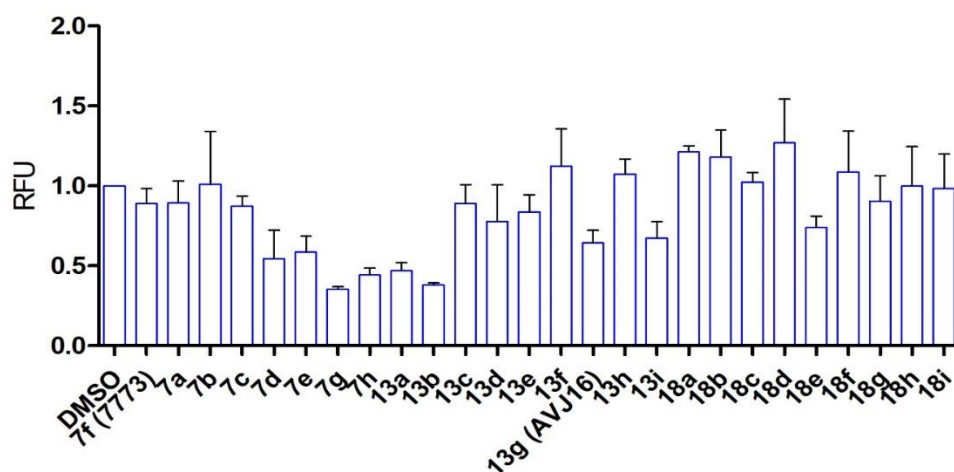


Figure 2. Screening of IGF2BP1 inhibitors. Bar graph showing split-luciferase assay to observe the inhibitory effect of **7773** and its analogs (**AVJ1-16**) on IGF2BP1 in transfected RKO cells. The RKO cells, 24 hours after transfection of reporter plasmids, were treated with **7773** and its analogs at a concentration of 0.5 μ M.

To select the most effective IGF2BP1 inhibitor among all synthesized compounds, the top nine active compounds reported in the above split-luciferase assay were brought forward for an analysis of cancer-linked properties in a cancer cell line. These compounds were tested in a wound healing assay using H1299 lung cancer cells, which express IGF2BP1 at a high level (Figure 3A). These cells had previously shown sensitivity in this assay to the lead compound **7773**.^[30] Five compounds, **7g**, **13g**, **13i**, **18e**, and **18g**, showed moderate to good inhibitory activity in the H1299 wound healing assay. These effects were quantified by calculating the IC_{50} for each compound. Compound **13g** outperformed the other compounds in inhibiting H1299 wound healing, with an

IC₅₀ of 0.7 μM, approximately 14 times more effective than **7773**, with an IC₅₀ of 10 μM (Table 1). To test for IGF2BP1 specificity, we compared the ability of these compounds to inhibit wound healing in mouse lung adenocarcinoma cells (LKR-M) that lack endogenous IGF2BP1 but have been transfected with either full length human IGF2BP1 (LKR-M-FI) or with GFP (LKR-M-GFP) as a control. Of the five compounds, only **13g** selectively inhibited wound healing in the LKR-M-FI cells without significantly inhibiting wound healing in the LKR-M-GFP control cells (Figure 3B; Supplemental Figure [1S2S](#)). Based on these findings, we identified compound **13g** as exhibiting remarkable specificity and proceeded to conduct subsequent experiments exclusively using this compound, which we designated as **AVJ16**.

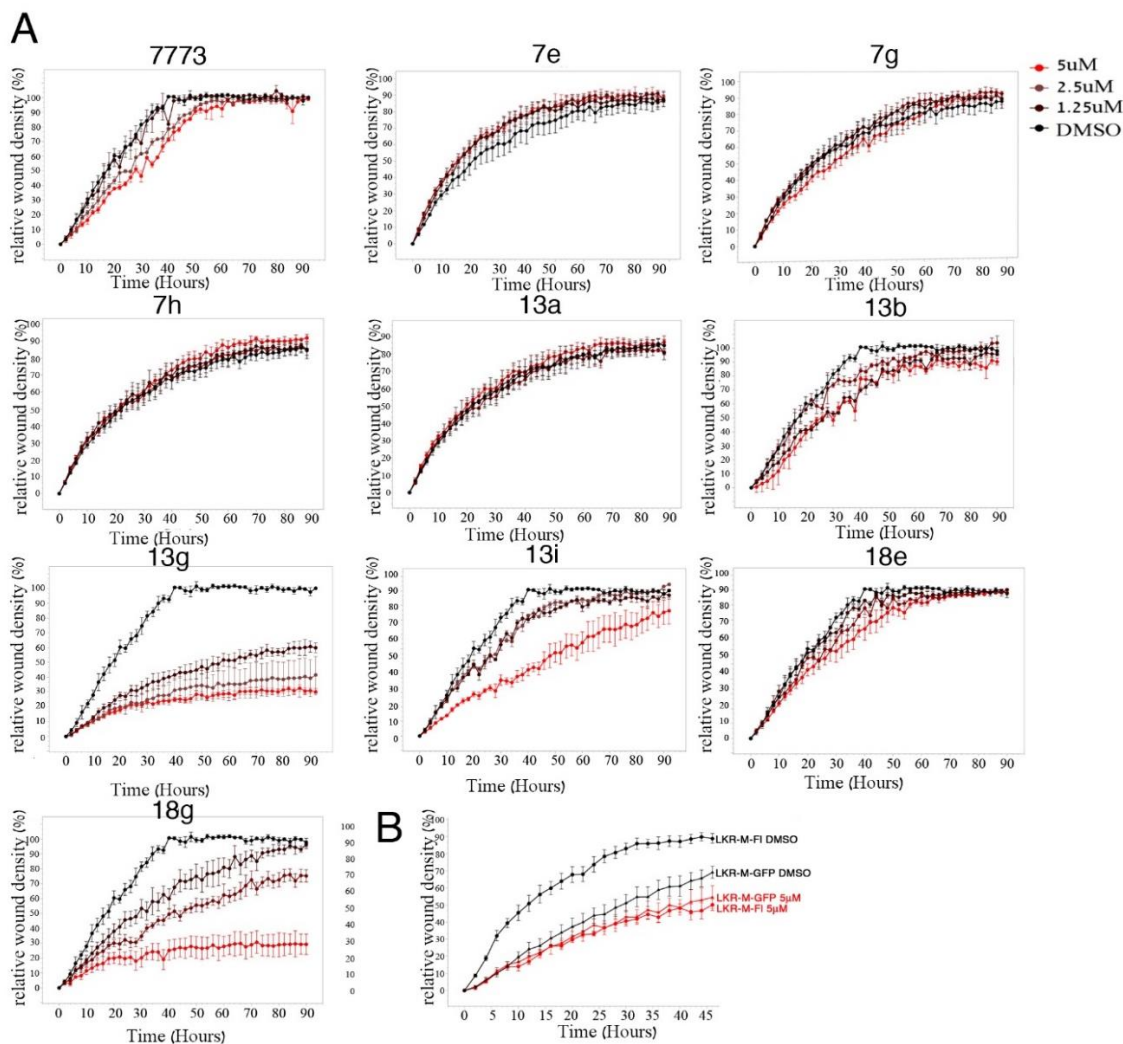


Figure 3. A. Screen of 7773 analogs. Compounds were screened against H1299 cells for their effect on inhibiting wound healing using the IncuCyte® S3 Live-Cell Analysis System. Each compound was tested in triplicate to calculate an IC₅₀. B. 5 μM **13g** (**AVJ16**) inhibits wound healing in LKR-M-FI when compared to DMSO (vehicle) treated cells but has little or no effect (compared to DMSO) on LKR-M-GFP cells.

Table 1: The IC₅₀ of the wound healing assay (H1299 cells)

Compounds ^a	IC ₅₀ (μM)
7e	20
7f (7773)	10
7g	10
7h	30
13a	>100
13b	>100
13g (AVJ16)	0.7
13i	4.5
18e	8
18g	2.5

^aTen of the newly synthesized molecules were screened in Incucyte wound healing and cell proliferation assays. The IC₅₀ of the wound healing assay for AVJ16 was 0.7 μM, as compared to 10 μM with 7773.

2.3.2. IGF2BP1 binding to AVJ16 and to compound 7773

We used MST to determine the strength of the interaction between the inhibitor **AVJ16** and the recombinant IGF2BP1 protein (Supplemental Figure [2S3S](#)). As can be observed in Figure 4A, **AVJ16** interacts with the protein with a K_d of ~1.4 μM, which is a 12-fold increase in binding over the lead compound **7773**.^[30] Next, we used the MST assay to directly test the inhibitory effect of **AVJ16** on IGF2BP1 binding to a target RNA. Kras6 is a 200bp sequence from the 3'UTR of KRAS mRNA IGF2BP1 targets that was used as the bait in our high throughput screen.^[30] 20 μM **AVJ16** completely inhibited binding of IGF2BP1 to Kras6 RNA compared to the DMSO control (Figure 4B). Electrophoretic mobility shift assays confirm that higher concentrations of IGF2BP1 are required for binding Kras6 RNA in the presence of **AVJ16** (Figure 4C).

Next, we tested the interaction between the **AVJ16** compound and IGF2BP1 KH34 di-domain using NMR. We first recorded a ¹⁵N-HSQC spectrum of the free IGF2BP1 KH34 sample and compared it with a previous spectrum, confirming that the protein sample was correctly folded (data not shown). Then, we titrated KH34 with increasing amounts of **AVJ16** and recorded NMR spectra at each titration point. Figure 4D reports the overlay of the spectra, which shows the

significant perturbation of several amide resonances of KH34, confirming the interaction of this di-domain with **AVJ16**.

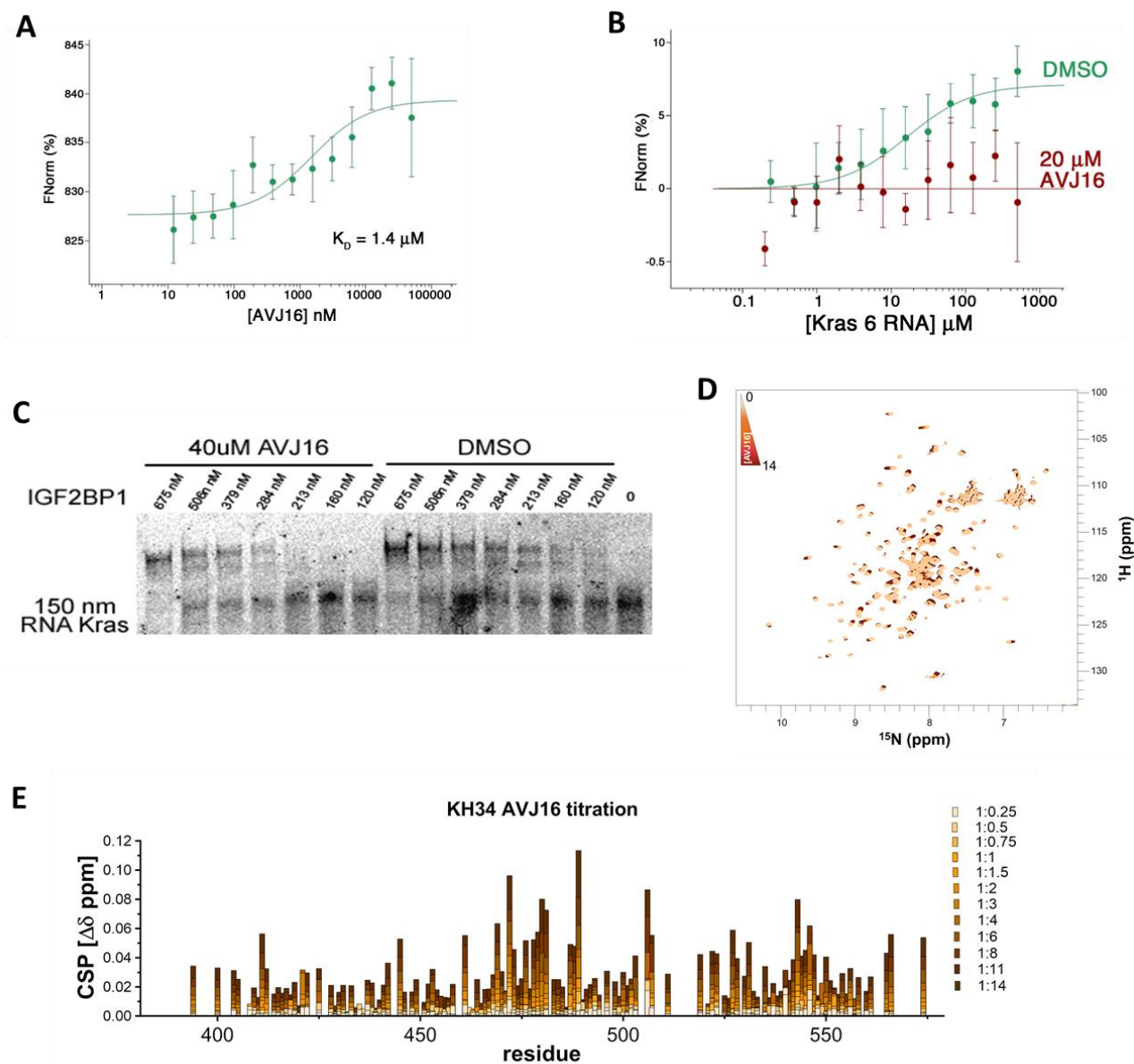


Figure 4. AVJ16 binding to IGF2BP1. (A) MST was used to determine the K_D of IGF2BP1 binding to **AVJ16**. (B) The ability of **AVJ16** to disrupt Kras6 RNA binding was assayed by MST. 20 μM **AVJ16** completely inhibited thermophoresis. (C) EMSA experiment comparing the effects of **AVJ16** vs. DMSO on IGF2BP1 binding to a fluorescent Kras6 RNA. When **AVJ16** is included in the binding reaction, higher concentrations of IGF2BP1 are required to achieve a gel shift than with DMSO. (D) Superimposition of a series of fingerprint ^{15}N -correlation NMR spectra obtained upon addition of increasing amounts of **AVJ16** to IGF2BP1 KH34 protein, as detailed in the methods section. The selective shifts of a group of resonances report on the interaction of the drug with the protein. (E)

Chemical shift perturbation (CSP) changes of the individual resonances in the spectra above are plotted against residue numbers.

To determine the **AVJ16** interaction surface on KH34, we transferred the previously reported assignment of human IGF2BP1 KH34 onto our ^1H - ^{15}N -HSQC NMR spectra, assigned the shifting amide-protons resonances and plotted the Chemical Shift Perturbations (CSPs) versus residue (Figure 4E). Next, in order to map **AVJ16** binding onto KH34, we focused on those residues that exhibited CSPs above three standard deviations of the average CSP at protein:compound molar ratio of 1:8 (Figure 5A). When compared to **7773**, **AVJ16** induces larger shifts at the same protein:RNA ratio (Figures 5B and C), indicating that the new compound has a greater affinity for the protein, consistent with what was observed using MST. Notably, the direction of the shifts observed for the two compounds is also similar. The mapping of the greater CSPs onto the structure of KH34 defines a semi-continuous binding surface at the interface of the two KH domains, similar to what was previously reported for **7773** (Figure 5D). Notably, a few amino acids with significant chemical shift changes are visible peripheral to the main binding surface (e.g. 461). These changes may be due to propagation of changes in structure and dynamics upon binding to the main surface, but also to secondary, we expect weaker, interactions.

Finally, to assess whether the previously reported specificity of IGF2BP1 KH34 targeting is maintained in **AVJ16**, we tested the interaction between the **AVJ16** and the human IGF2BP1 KH12 di-domain. As for KH34, we first recorded a ^{15}N -HSQC spectrum of the free IGF2BP1 KH12 sample and then we titrated in increasing amounts of **AVJ16**. In contrast to KH34, only negligible shifts were observed, confirming that, as for **7773**, the **AVJ16** compound does not interact with KH12 (Figure 5E). These results are confirmed by a further MST analysis that shows that AVJ16 binds to KH34 with a K_d of ~840 nM but does not associate with KH12 (Figure 5F).

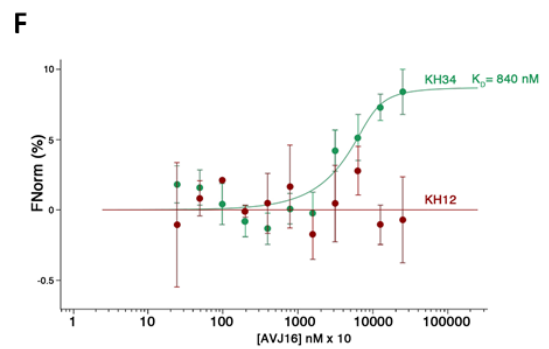
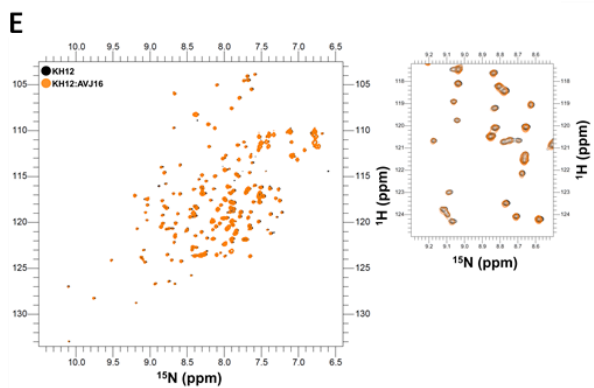
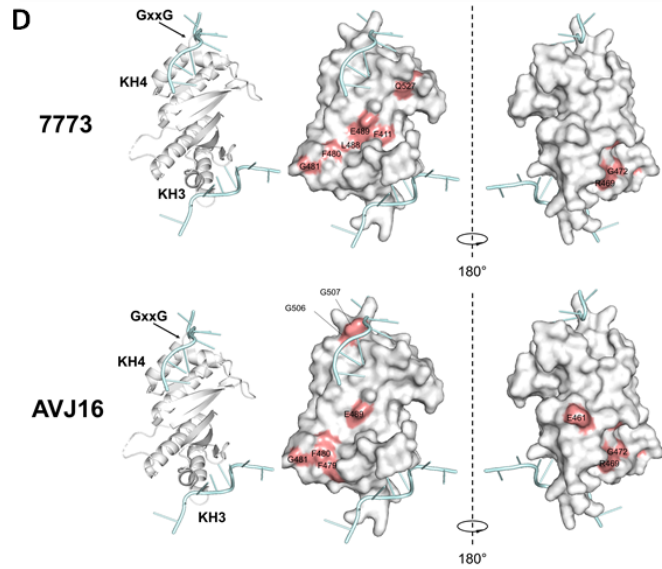
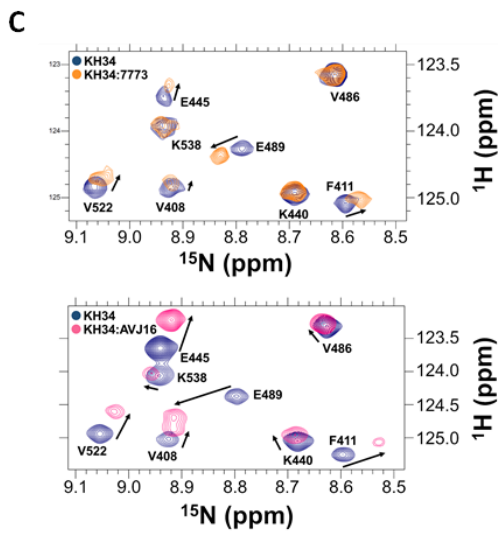
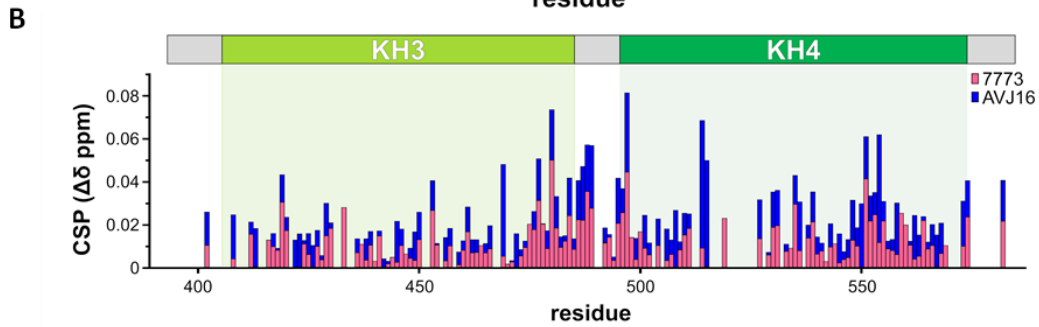
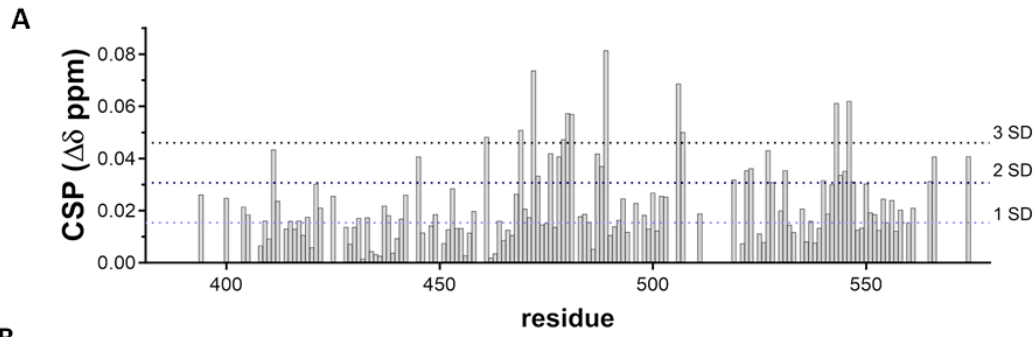


Figure 5. AVJ16 binding comparison with 7773. (A) KH34 per-residue chemical shift perturbations (CSP) recorded upon 1:8 AVJ16 binding. The dotted lines indicate, respectively, one (light blue), two (blue) and three (violet) standard deviations of the average CSP observed. (B) CSP vs residue plots of **7773** and **AVJ16** on KH34. The overall magnitude of the CSP observed, at the same protein:drug molar ratio (1:8), is greater for **AVJ16**. (C) Zoom-in in the window of ^1H 8.45–9.12 ppm and ^{15}N 124–125.5 ppm, showing that the same residues are shifting further but in the same direction upon addition of **AVJ16**. (D) Mapping comparison of **7773** and **AVJ16** on KH34. The affected residues (>3 SD) are depicted in salmon. (E) AVJ16 binding to IMP1 KH12. The left panel reports the whole spectrum of KH12 in its apo form and upon addition of 1:4 molar ratio of **AVJ16**. Only very small shifts were observed. The right panel reports a magnification of the region between ^1H 8.5–9.25 ppm and ^{15}N 115–130. (F) MST analysis of AVJ16 binding to KH12 and KH34.

2.3.3. AVJ16 treatment leads to a downregulation of IGF2BP1 target RNAs, including Kras RNA and protein

IGF2BP1 has been observed to stabilize a variety of cancer-associated RNA targets by binding to coding or non-coding sequences in mRNA. Having demonstrated AVJ16's ability to bind directly to IGF2BP1 and interfere with RNA binding in vitro, we assessed how the inhibitor affects target RNAs in vivo. We performed quantitative PCR (qPCR) analysis of steady state levels of several cancer-associated RNAs known to be IGF2BP1 targets (Figure 6). Treatment of H1299 cells with a low concentration (1.5 μM) of AVJ16 for 48 hours led to a decrease in steady state levels of most of the assayed RNAs, although the extent of reduction varied among the different transcripts. No effect on these mRNAs was observed when examined in AVJ16-treated RKO cells (Figure 6A, B). In particular, Kras mRNA is downregulated by approximately 50% as a result of 48 hours of AVJ16 treatment. Because Kras mRNA fragment was used as the probe for the initial high throughput screen, we examined more closely the effect of AVJ16 on Kras in H1299 cells. At 24 hours, Kras protein levels are reduced in a dose-dependent manner (Figure 6C), and the reduction in Kras protein is maintained in these cells for up to 4 days. AVJ16 thus appears to sensitize several IGF2BP1 target RNAs to degradation within IGF2BP1-expressing cells.

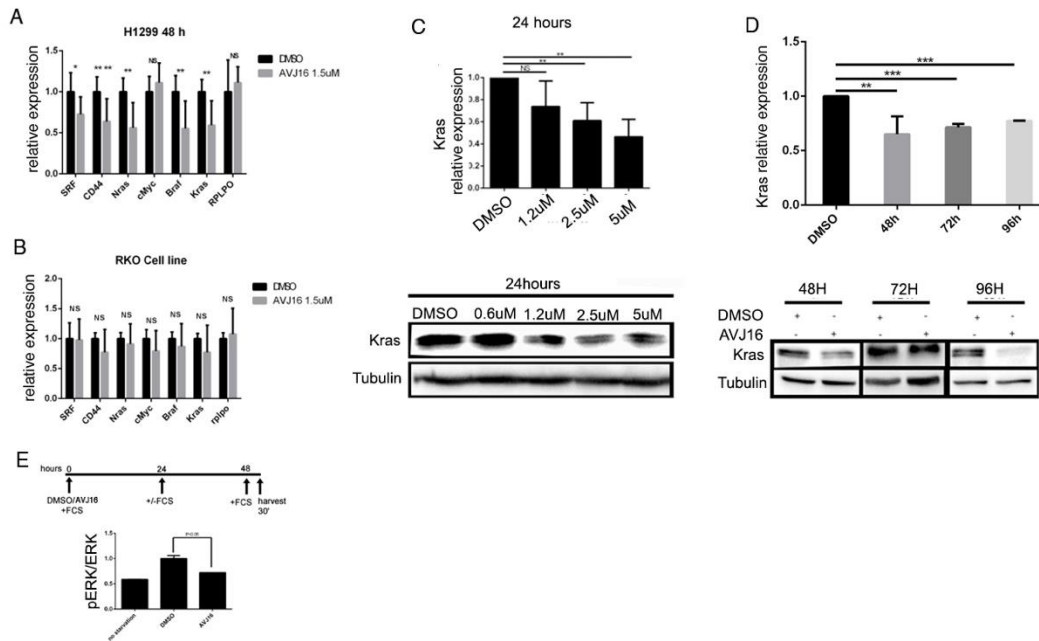


Figure 6. **AVJ16** downregulates **Kras** and other **IGF2BP1** target RNAs, **Kras** RNA and protein. (A) Real-time PCR analysis of steady state levels of **SRF**, **CD44**, **Nras**, **cMyc**, **Braf**, and **Kras** RNA in H1299 cells treated with either 1.5 μ M **AVJ16** (Gray) or **DMSO** (Black) for 48 hours. (B) Real time PCR analysis for the same genes in non-**IGF2BP1** expressing **RKO** cell line. (C) Western blot analysis of **Kras** expression in H1299 cells incubated in 1.2 μ M, 2.5 μ M, or 5 μ M **AVJ16**, or **DMSO** for 24 hours. Triplicates were performed and analysed for each concentration. **Tubulin** was used as loading control and for quantification of the blot (bottom panel). (D) H1299 cells were cultured with 4 μ M **AVJ16** or **DMSO** for 48, 72 and 96 hours. Triplicates were performed and analysed for each concentration. **Tubulin** was used as loading control and for quantification of the blot (bottom panel). (E) H1299 cells were cultured with either 1.5 μ M **AVJ16** or **DMSO** for 24 hours, after which **FCS** was removed from the medium and the cells were cultured for another 24 hours. At that point, **FCS** was re-added for 30' and then protein extracts were prepared and analyzed by western blot for expression of **ERK** and phospho**ERK** (**pERK**). Cells grown continuously in **FCS** for 48.5 hours were used as controls. The ratio of **pERK** to **ERK** was calculated for each sample by digital analysis of the gels.

2.3.4. AVJ16 inhibits tumorigenic properties of cancer cells in IGF2BP1-dependent manner

To determine the effect of **AVJ16** on **IGF2BP1**-dependent inhibition of cell proliferation, we treated both **IGF2BP1** overexpressing cells and cells that do not express the gene with **AVJ16**. **AVJ16** inhibited proliferation of **LKR-M-FI** cells in a dose dependent manner, with even low concentrations, such as 1.25 μ M, having considerable and significant effect (Figure 7A). Strikingly, **AVJ16** did not affect cell growth in **LKR-M-GFP** cells that do not express **IGF2BP1** (Figure 7B), suggesting not only that **AVJ16** is highly specific for **IGF2BP1** but also not toxic in these cells. **AVJ16** also inhibited cell proliferation in a dose-dependent manner in the human lung

cancer cell line H1299 that endogenously expresses IGF2BP1, with 5 μ M and 1.25 μ M concentrations sufficient to significantly inhibit cell growth (Figure 7C).

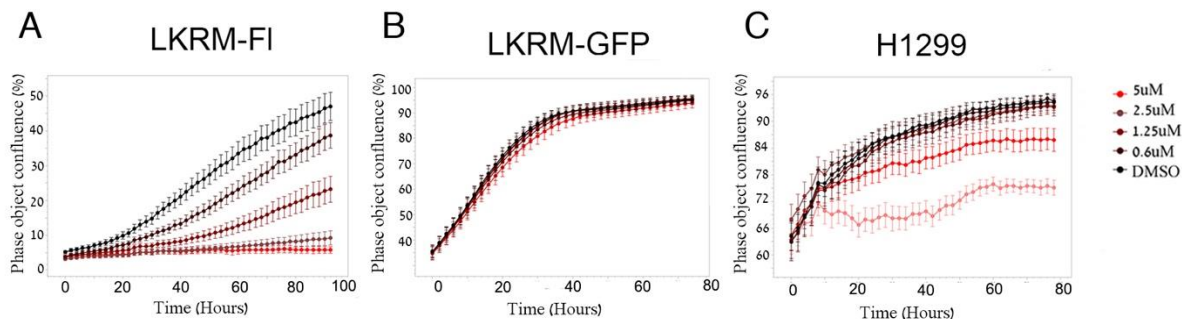


Figure 7. **AVJ16** inhibits cell proliferation in mouse/human lung carcinoma cells only when they express IGF2BP1. LKR-M cells, that do not express endogenous IGF2BP1, were transfected with either full length IGF2BP1 (LKR-M-FI) (A) or with GFP alone (LKR-M-GFP) (B) and assayed for cell proliferation in the presence of DMSO (vehicle) or the indicated concentrations of **AVJ16**. (C) The human lung cancer cell line H1299 that expresses endogenous IGF2BP1 was assayed for cell proliferation at the indicated concentrations of **AVJ16**.

To validate the efficacy and specificity of compound **AVJ16** in another cancer cell type, we utilized human CRC cell lines with high (HCT116) and low/no (RKO) expression of IGF2BP1. We have observed a significant dose-dependent decrease in the proliferation of HCT116 cell lines compared to RKO cells, consistent with a specific inhibitory effect of compound **AVJ16** on IGF2BP1 (Figure 8A). Furthermore, we have shown that compound **AVJ16** induced apoptosis in a dose-dependent manner in HCT116 and SW480 cells, that expresses IGF2BP1, but not in RKO cells, which do not (Figure 8B). Finally, we observed significant inhibition in the migration of SW480 wild-type cells but not in SW480 IGF2BP1 knockout cells (Figure 8C), even upon treatment with a lower dose of compound **AVJ16** (2 μ M) (Figure 8D and E). These results suggest the high potency and specificity of analog **AVJ16** for the IGF2BP1-dependent inhibition of pro-tumorigenic phenotypes not only in lung adenocarcinoma cells but also in CRC cells.

3. Discussion

We conducted a structure–activity relationship (SAR) study based on the lead "7773" structure to optimize this compound and produce more selective, potent, and safe small-molecule inhibitors of IGF2BP1 that could be clinically developed as cancer therapeutics. By modifying or

substituting rings A, B, and C (Figure 1) of the parent lead molecule **7773**, 25 new compounds were produced (Schemes 1-3). The lead compound's fundamental skeleton and overall length were retained in the new molecules in an effort to preserve the active site binding while improving the binding potential. Our newly-developed cell-based split-luciferase assay, designed to determine effectiveness at preventing the formation of IGF2BP1 homodimers on target RNA in cells, was used for the initial screen of newly produced analogs to test IGF2BP1 inhibition. This test revealed a number of compounds that performed equally well or better than lead **7773**. Based on this initial screen, that is designed to assess ability of IGF2BP1 to dimerize, the selected compounds were subjected to further functional analysis. Since IGF2BP1 is known to assist cancer cell migration, we tested the impact of the top nine of these compounds on the migration of the IGF2BP1-expressing H1299 lung cancer cell line. **AVJ16** was identified as a potent inhibitor with an IC_{50} of 0.7 μ M compared to **7773** with an IC_{50} of 10 μ M, suggesting this compound's high inhibitory effect.

Importantly, MST analysis was used to confirm the direct binding of **AVJ16** to IGF2BP1 and showed a 12-fold improvement in binding compared to the lead compound (K_D of 1.4 μ M vs. 17 μ M for "**7773**"), and EMSA assays indicated an increased inhibition of IMP1 binding to Kras mRNA, an important cancer target.

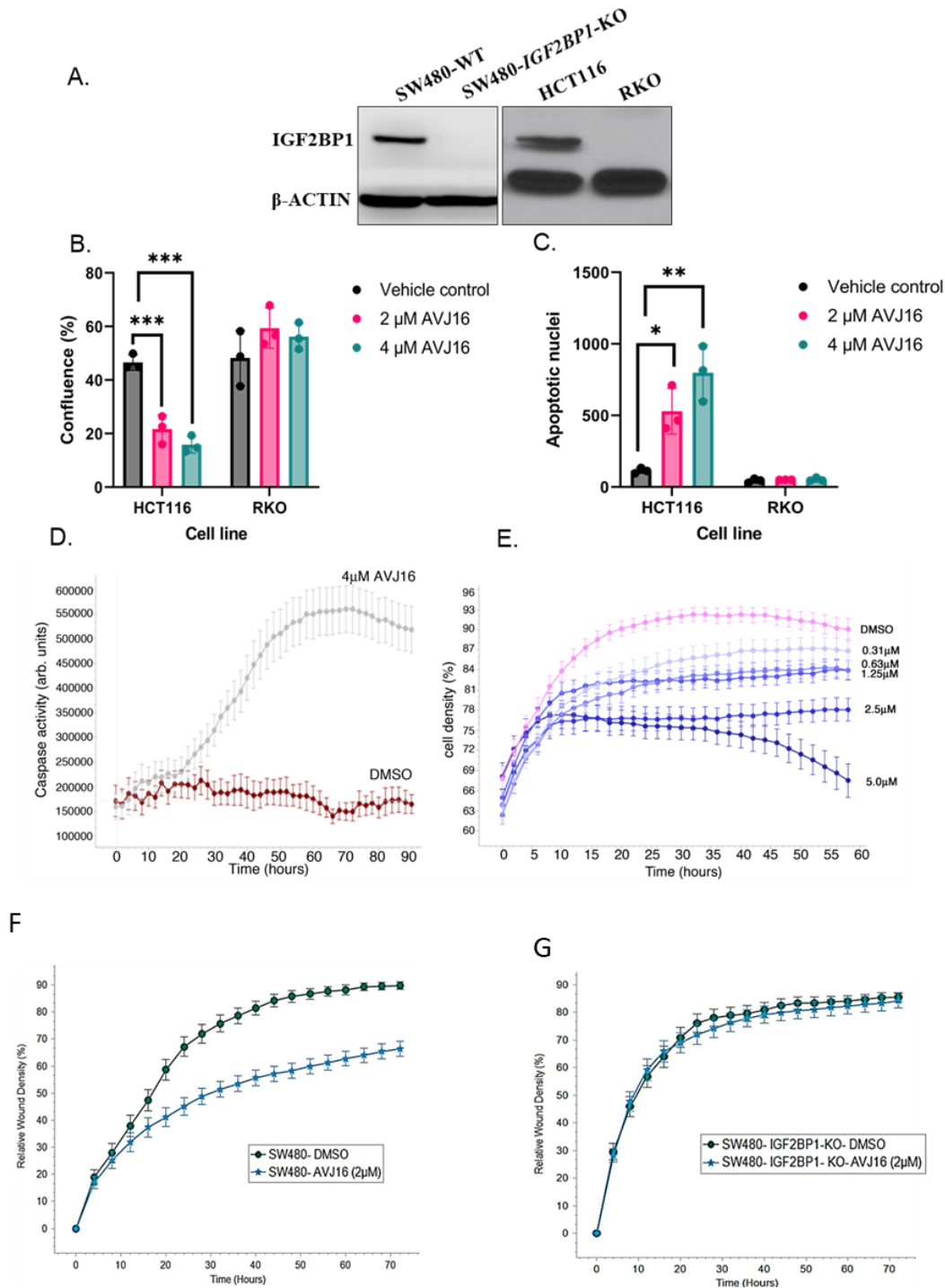


Figure 8. Colorectal cell lines showing IGF2BP1 specific sensitivity towards compound **AVJ16**. (A) Immunoblot assay showing expression of IGF2BP1 in SW480-WT, HCT116 cells versus its absence in RKO and SW480-IGF2BP1-KO cells. Beta-actin antibody was used for normalization. (B) Bar graph showing dose dependent inhibitory effect of compound **AVJ16** on the proliferation of HCT116 cells, while RKO cells do not show inhibitory effect. (C) Bar graph showing increase in Apoptotic nuclei with increase in the concentration of compound **AVJ16** in HCT116 cells, while RKO cells did not show significant change with increase in the dose concentration. (D) SW480 cells treated with 4 μ M AVJ16 show a sharp increase in apoptosis-associated Caspase 3/7 staining after 20 hours and (E) a

drop in cell density after 36 hours. (F) and (G) A significant decrease in wound healing is observed upon treatment with **AVJ16** (2 μ M) in SW480-wild type cells, while insignificant change was observed in case of SW480-IGF2BP1-Knockout cells.

Our NMR data indicated that, as expected, titration of the KH34 di-domain with **AVJ16** resulted in larger peak shifts compared to **7773**, confirming the higher affinity of the former. Notably, most of the peaks shifting in the **7773** and **AVJ16** titrations are the same, and the direction of the peak shifts is also very similar, indicating that the two compounds bind very similarly. The minor local differences we observe are expected, given the difference in the structure of the two compounds. Moreover, NMR data indicate that AVJ16, like **7773**, binds to the KH34 di-domain of the protein, in an hydrophobic patch, at the interface between KH3 and KH4 domains, rather than in the KH domains' nucleic acid binding groove. This surface is built by arranging two KH domains in an antiparallel pseudo-dimer, and the details of this arrangements are unique for KH34. Indeed, neither **7773** nor **AVJ16** binds to IGF2BP1 KH12, where the KH1 and KH2 domains are also arranged in an antiparallel pseudo-dimer but where the shape and composition of the joining surface is different[33]. This confirms the potential of this surface to develop unique interactions between a low molecular weight compound and the protein.

Recently, we demonstrated that genetically inhibiting IGF2BP1 hinders metastasis of LUAD and melanoma tumors.[20, 34] To investigate the cellular functions of **AVJ16** as an IGF2BP1 inhibitor, we analyzed its effect on proliferation, survival, and migration of LUAD and CRC cells. IGF2BP1-expressing mouse LKR-M lung cancer cells and human SW480 colon cancer cells exhibited inhibition in proliferation and migration of cells. No inhibition, however, of proliferation or migration was observed with control LKR-M-GFP and SW480-IGF2BP1-knockout cells, demonstrating the specificity of **AVJ16**. Two additional colon cancer cell lines, HCT116 (IGF2BP1 positive) and RKO (IGF2BP1 negative), further verified **AVJ16** potency and specificity. In cell culture, this new compound was shown to be highly specific and about 12 times more potent than the lead molecule **7773**, causing a reduction in many IGF2BP1 target mRNAs, including Kras. Together, our data provide compelling evidence that **AVJ16** is effective and selective in inhibiting IGF2BP1 function in cancer cells. Earlier, we reported that the downregulation of IGF2BP1 makes melanoma, neuroblastoma and CRC cells more susceptible to chemotherapeutic drugs and targeted therapy, [5, 14-16, 18, 35] thus making it an attractive target for developing novel therapeutics. High-throughput screening against novel targets followed by

structural optimizations and preclinical/clinical testing have resulted in several cancer drugs such as erlotinib. Similarly, to develop AVJ16 further, future studies will establish its effectiveness, alone or in combination with other anti-cancer modalities, *in vivo* for further development of potential anti-cancer and anti-metastatic therapies. Furthermore, AVJ16 and its derivatives are not only promising candidates as cancer therapeutics but are also valuable tool compounds that can be used to study the biology of IGF2BP1 *in vitro* and *in vivo*.

4. EXPERIMENTAL SECTION

4.1. Chemistry

Melting points were recorded on a Fischer-Johns melting point apparatus and are uncorrected. ¹H-NMR and ¹³C-NMR spectra were recorded on a Bruker Advance 500 instrument in either DMSO, CDCl₃ and MeOH-d₄ operating at 500 and 125 MHz, respectively. Chemical shifts are reported in δ values (ppm) and *J* values are reported in hertz (Hz). The signals are quoted as s (singlet), d (doublet), t (triplet), and m (multiplet), and dd (doublet of doublet). High resolution (ESI or EI) MS were carried out at the Penn State Metabolomics Facility - University Park, PA. Experiments involving moisture and/or air sensitive components were performed under a nitrogen atmosphere in oven-dried glassware. Reagents, starting materials, and anhydrous solvents were purchased from commercial suppliers and were used as received. Reaction courses were monitored by thin-layer chromatography (TLC) on pre-coated silica gel 60 F254 aluminum sheets (Merck, Darmstadt, Germany), and the spots were visualized under UV light. The crude reaction products were purified by silica gel column chromatography using silica gel 60 Å (Merck, 230-400 mesh). The intermediate **4**, **11**, **16** was synthesized following a literature method. The purity of the final compounds (97%) was quantified by analytical high-performance liquid chromatography analysis by comparing the peak areas of the product relative to any impurities.

4.1.1. Synthesis of precursor **6**, **12** and **17**

To a stirred solution of intermediate **4** (100mg, 0.29 mmol) and triethyl amine (0.17 mL, 1.18 mmol) in dry THF (10 mL), acid chloride **5** (69 mg, 0.29 mmol) was added dropwise at 0 °C and the reaction mixture was stirred at same temperature for 1h. The progress of the reaction was monitored by TLC. After the completion of the starting materials, water was added, and the

compound was extracted with ethyl acetate (15 mL × 3). The combined organic layers were dried over sodium sulphate and concentrated under reduce pressure to obtained the compound which was used for the next step without further purification. The same procedure was repeated for the synthesis of precursor **12** and **17**.

4.1.2. General procedure for the synthesis of compounds **7a-g**

To a stirred solution of various heterocycles (1eq), in dry acetonitrile (10 mL), K₂CO₃ (1.2 eq) was added, and the reaction mixture was stirred for 15 min at room temperature. Precursor **6** (1.2 eq) was added portion wise to above mixture and the RM was stirred at reflux for 3h. Progress of the reaction was monitored by TLC. After the completion of the reaction, water was added, and the compound was extracted with ethyl acetate. The combined organic layer was dried over anhydrous sodium sulphate and concentrated to obtain the crude mass which was purified using silica gel as a stationary phase and 3:7 (MeOH:CH₂Cl₂) mixture as an eluent.

(3-(Benzo[d][1,3]dioxol-5-ylamino)piperidin-1-yl)(4-(morpholinomethyl)phenyl)methanone (**7a**). White solid. mp 66-68 °C. ¹H NMR (500 MHz, DMSO-*d*₆) δ 1.45-1.56 (m, 2H), 1.66-1.81 (m, 1H), 1.98-2.00 (m, 1H), 2.35 (s, 4H), 2.75 (s, 1H), 3.06 (t, *J*=10.5 Hz, 1H), 3.22-3.24 (m, 1H), 3.43-3.50 (m, 3H), 3.58 (s, 5H), 5.22 (s, 1H), 5.76-5.79 (m, 3H) 6.21 (s, 1H), 6.38-6.44 (m, 1H), 7.31-7.37(m, 4H). ¹³C NMR (125 MHz, DMSO-*d*₆) δ 23.5, 30.9, 42.3, 49.5, 51.9, 53.6,62.5, 66.6, 95.9, 100.4, 103.6, 108.6, 126.9, 127.4, 129.1, 135.5, 138.4, 139.4, 143.3, 148.2, 169.9. HRMS calcd for C₂₄ H₂₉N₃O₄ 423.2158, found [M + H]⁺ 424.2233.

(3-(Benzo[d] [1,3] dioxol-5-ylamino)piperidin-1-yl) (4-(pyrrolidin-1-ylmethyl) phenyl) methanone (**7b**): Off white solid. Yield: 72%. mp 90-92 °C. ¹H NMR (500 MHz, DMSO-*d*₆), 1.47-1.56 (m, 2H), 1.79 (s, 6H), 2.00-2.01 (m, 2H), 2.67 (s, 4H), 2.76 (t, *J*=10 Hz, 1H), 3.05-3.10 (m, 2H), 3.82 (s, 2H), 5.07 (d, *J*=5.0 Hz, 1H), 5.81 (s, 2H), 5.94 (s, 1H), 6.25 (s, 1H), 6.56 (s, 1H), 7.36 (d, *J*=10Hz, 2H), 7.42 (d, *J*=5.0 Hz, 2H), ¹³C NMR (125 MHz, DMSO-*d*₆), 23.51, 31.12, 49.9, 53.7, 58.9, 96.1, 100.4, 104.2, 108.7, 127.1, 129.3, 136.0, 138.6, 143.4, 148.3, 169.8. HRMS calcd for C₂₄ H₂₉N₃O₃ 407.2209, found [M + H]⁺ 408.2283.

(4-((1*H*-Imidazol-1-yl)methyl)phenyl)(3-(benzo[d][1,3]dioxol-5-ylamino)piperidin-1-yl)methanone (**7c**). Off white solid. Yield: 68%. mp 180-182 °C. ¹H NMR (500 MHz, DMSO-*d*₆)

δ 1.46-1.50 (m, 2H), 1.75 (s, 1H), 1.98-2.00 (m, 1H), 2.74 (s, 1H), 3.03-3.08 (m, 2H), 3.24 (s, 1H), 5.05 (s, 1H), 5.23 (s, 2H), 5.82-5.83 (m, 2H), 5.93 (s, 1H), 6.23 (s, 1H), 6.55 (s, 1H), 6.93 (s, 1H), 7.15 (s, 1H), 7.26 (d, $J=7.5$ Hz, 2H), 7.38 (d, $J=7.5$ Hz, 2H), 7.72 (s, 1H). ^{13}C NMR (125 MHz, DMSO- d_6), δ 23.9, 29.5, 31.1, 49.7, 49.8, 65.2, 96.0, 100.4, 104.3, 108.8, 120.0, 127.5, 127.7, 129.2, 136.3, 137.9, 138.6, 139.2, 143.6, 148.3, 169.5. HRMS calcd for $\text{C}_{23}\text{H}_{24}\text{N}_4\text{O}_3$ 404.1848, found $[\text{M} + \text{H}]^+$ 405.1923.

(4-((1H-1,2,4-Triazol-1-yl) methyl) phenyl) (3-(benzo[d] [1,3] dioxol-5-ylamino) piperidin-1-yl) methanone (**7d**). Off white solid. Yield: 68%. mp 83-85 °C. ^1H NMR (500 MHz, DMSO- d_6) δ 1.46-1.54 (m, 2H), 1.75 (s, 1H), 1.99-2.01 (m, 1H), 2.74-2.76 (m, 1H), 3.03-3.08 (m, 1H), 3.23-3.24 (m, 2H), 5.05 (d, $J=10$ Hz, 1H), 5.45 (s, 2H), 5.83 (s, 2H), 5.92 (s, 1H), 6.23 (s, 1H), 6.54 (s, 1H), 7.30 (d, $J=5.0$ Hz, 2H), 7.39 (d, $J=10$ Hz, 2H), 7.97 (s, 1H), 8.60 (s, 1H), ^{13}C NMR (125 MHz, DMSO- d_6) δ 23.8, 31.09, 49.8, 52.3, 96.0, 100.4, 104.3, 108.8, 127.4, 128.1, 136.5, 137.7, 138.7, 143.6, 144.7, 148.3, 152.1, 169.5. HRMS calcd for $\text{C}_{22}\text{H}_{23}\text{N}_5\text{O}_3$ 405.1801, found $[\text{M} + \text{H}]^+$ 406.1877.

(3-(Benzo[d][1,3]dioxol-5-ylamino)piperidin-1-yl)(4-((3-nitro-1H-1,2,4-triazol-1-yl)methyl)phenyl)methanone (**7e**). Yellow solid. Yield: 65%. mp 95-97 °C. ^1H NMR (500 MHz, DMSO- d_6) δ 1.45-1.51 (m, 2H), 1.75-1.79 (m, 1H), 1.98-2.00 (m, 1H), 2.76 (s, 1H), 3.06-3.11 (m, 2H), 3.24 (s, 1H), 5.04-5.05 (m, 1H), 5.60 (s, 2H) 5.79-5.81 (m, 3H), 6.22 (s, 1H), 6.51 (s, 1H), 7.41 (s, 4H), 8.95 (s, 1H), ^{13}C NMR (125 MHz, DMSO- d_6) δ 23.4, 30.8, 42.3, 49.3, 51.7, 53.8, 95.8, 100.4, 103.6, 108.5, 127.5, 128.6, 137.0, 38.4, 147.4, 148.1, 162.8. HRMS calcd for $\text{C}_{22}\text{H}_{22}\text{N}_6\text{O}_5$ 450.1652 found $[\text{M} + \text{H}]^+$ 451.1728.

(3-(Benzo[d][1,3]dioxol-5-ylamino)piperidin-1-yl)(4-(selenocyanatomethyl)phenyl) methanone (**7g**). To a stirred solution of compound **6** (1 eq) in dry acetonitrile, KSeCN (1.2 eq) was added and the reaction mixture was stirred for 17h at reflux. The progress of the reaction was monitored by thin layer chromatography. After the completion of the reaction, water was added, and the compound was extracted with ethyl acetate. The combined organic layer was dried over anhydrous sodium sulphate and concentrated under reduce pressure to get the crude mass. The compound was purified using flash chromatography and 3% MeOH: CH_2Cl_2 as an eluent. Off white solid. Yield: 54%. mp 62-65 °C. ^1H NMR (500 MHz, DMSO- d_6) δ 1.47-1.56 (m, 2H), 1.76

(s, 1H), 2.00-2.02 (m, 1H), 2.78 (t, $J=10$ Hz, 1H), 3.06-3.11 (m, 2H), 3.25-3.28 (m, 2H), 4.37 (s, 2H), 5.82 (s, 2H), 5.98 (s, 1H), 6.26 (s, 1H), 6.59 (s, 1H), 7.39-7.44 (m, 4H). ^{13}C NMR (125 MHz, DMSO- d_6) δ 24.1, 31.0, 32.6, 49.9, 96.2, 100.4, 104.5, 108.8, 127.4, 129.2, 136.3, 138.8, 139.6, 143.5, 148.3, 169.5. HRMS calcd for $\text{C}_{21}\text{H}_{21}\text{N}_3\text{O}_3\text{Se}$ 443.0748 found $[\text{M} + \text{H}]^+$ 444.0822.

1-(4-(3-(Benzo[d][1,3]dioxol-5-ylamino)piperidine-1-carbonyl)benzyl)thiourea (7h). To a stirred solution of compound **6** (1 eq) in dry acetonitrile, thiourea (1.2 eq) was added and the reaction mixture was stirred for 17h at reflux. The progress of the reaction was monitored by thin layer chromatography. After the completion of the reaction, white solid material in the reaction was filtered off and washed with ether to get the pure compound **7i**. Off white solid, Yield: 62%. mp 212-213 °C. ^1H NMR (500 MHz, DMSO- d_6) δ 1.46-1.51 (m, 2H), 1.75-1.78 (m, 1H), 1.99-2.00 (m, 1H), 2.76 (s, 1H), 3.07-3.11 (m, 5H), 4.52 (s, 2H), 5.07 (s, 1H), 5.82 (m, 2H), 5.93 (s, 1H), 6.24 (s, 1H), 6.56 (s, 1H), 7.40 (d, $J=8.0$ Hz, 2H), 7.45 (d, $J=8.0$ Hz), 9.00 (s, 1H). ^{13}C NMR (125 MHz, DMSO- d_6) δ 9.1, 24.0, 31.0, 34.6, 46.5, 49.8, 55.2, 96.1, 100.4, 104.3, 108.8, 127.6, 129.3, 136.6, 138.7, 143.6, 148.3, 169.4, 169.6. HRMS calcd for $\text{C}_{21}\text{H}_{24}\text{N}_4\text{O}_3\text{S}$ 412.1569, found $[\text{M} + \text{H}]^+$ 413.1642.

4.1.3. General procedure for the synthesis of compounds **13a-i**

Compounds **13a-i** were synthesized following procedure mentioned for the synthesis of **7a-h**.

(4-(Benzo[d][1,3]dioxol-5-yl)piperazin-1-yl)(4-(morpholinomethyl)phenyl)methanone (13a). Off white solid. Yield: 68%. mp 43-45 °C. ^1H NMR (500 MHz, DMSO- d_6) δ 2.37 (s, 4H), 3.03 (s, 4H), 3.51 (s, 4H), 3.58-3.60 (m, 4H), 3.73 (s, 2H), 5.93 (s, 2H), 6.37 (dd, $J_{1,2}=5.0$ Hz, $J_{1,3}=10.0$ Hz, 1H), 6.70-6.71 (m, 1H), 6.78 (d, $J=10$ Hz, 1H), 7.39 (s, 4H). ^{13}C NMR (125 MHz, DMSO- d_6) δ 50.6, 53.6, 62.4, 66.6, 100.30, 101.1, 108.5, 109.1, 127.4, 129.2, 134.9, 140.0, 141.4, 147.3, 148.3, 169.4. HRMS calcd for $\text{C}_{23}\text{H}_{27}\text{N}_3\text{O}_4$ 409.2002, found $[\text{M} + \text{H}]^+$ 410.2074.

(4-(Benzo[d][1,3]dioxol-5-yl)piperazin-1-yl)(4-(pyrrolidin-1-ylmethyl)phenyl)methanone (13b). Off white solid, Yield: 62%. mp 201-213 °C. ^1H NMR (500 MHz, CDCl_3) δ 2.61 (s, 4H), 3.00-3.14 (m, 8H), 3.56 (s, 2H), 3.93 (s, 2H), 4.21 (s, 2H), 5.93 (s, 2H), 6.38 (d, $J=7.0$ Hz, 1H),

6.57 (s, 1H), 6.74 (d, $J=8.5$ Hz, 1H), 7.52 (d, $J=8.0$ Hz, 2H), 7.75 (d, $J=8.0$ Hz, 2H). ^{13}C NMR (125 MHz, CDCl_3): δ 23.1, 42.3, 47.7, 51.2, 53.3, 58.2, 100.7, 101.0, 108.2, 109.9, 128.1, 130.6, 137.0, 142.3, 146.8, 148.3, 169.3. HRMS calcd for $\text{C}_{23}\text{H}_{27}\text{N}_3\text{O}_3$ 393.2052, found $[\text{M} + \text{H}]^+$ 394.2126.

(4-((1H-Imidazol-1-yl)methyl)phenyl)(4-(benzo[d][1,3]dioxol-5-yl)piperazin-1-yl)methanone (13c) Off white solid. Yield: 70%. mp 135-137 °C, ^1H NMR (500 MHz, CDCl_3) δ 4.29-3.12 (m, 4H), 3.56 (s, 2H), 3.93 (s, 2H), 5.18 (s, 2H), 5.92 (s, 2H), 6.37 (dd, $J_{1,2}=2.0$ Hz, $J_{1,3}=8.5$ Hz, 1H), 6.56 (d, $J=2.5$ Hz, 1H), 6.74 (d, $J=8.5$ Hz, 1H), 6.94 (s, 1H), 7.15 (s, 1H), 7.22 (d, $J=8.0$ Hz, 2H), 7.45 (d, $J=8.0$ Hz, 2H), 7.61 (s, 1H). ^{13}C NMR (125 MHz, CDCl_3): δ 42.3, 47.7, 50.4, 51.6, 100.6, 101.0, 108.2, 109.8, 119.3, 127.3, 127.8, 129.9, 137.7, 137.4, 137.9, 142.3, 146.8, 148.3, 169.6. HRMS calcd for $\text{C}_{22}\text{H}_{22}\text{N}_4\text{O}_3$ 390.1692; found $[\text{M} + \text{H}]^+$ 391.1768.

(4-((1H-1,2,4-Triazol-1-yl)methyl)phenyl)(4-(benzo[d][1,3]dioxol-5-yl)piperazin-1-yl)methanone (13d). Off white solid. Yield: 80%. mp 142-143 °C, ^1H NMR (500 MHz, CDCl_3), δ 2.98–3.13 (m, 4H), 3.56 (s, 2H), 3.93 (s, 2H) 5.41 (s, 2H), 5.93 (s, 2H), 6.38 (d, $J=7.5$ Hz, 1H), 6.57 (s, 1H), 6.74 (d, $J=8.5$ Hz, 1H), 7.33 (d, $J=8.0$ Hz, 2H), 7.46 (d, $J=8.0$ Hz, 2H), 8.01 (s, 1H), 8.14 (s, 1H). ^{13}C NMR (125 MHz, CDCl_3): δ 42.2, 47.7, 51.3, 51.6, 53.1, 100.7, 101.0, 108.2, 109.9, 127.9, 128.0, 136.0, 136.4, 142.4, 143.2, 146.8, 148.3, 152.4, 169.5. HRMS calcd for $\text{C}_{21}\text{H}_{21}\text{N}_5\text{O}_3$ 391.1644, found $[\text{M} + \text{H}]^+$ 392.1716.

(4-(Benzo[d][1,3]dioxol-5-yl)piperazin-1-yl)(4-((3-nitro-1H-1,2,4-triazol-1-yl)methyl)phenyl)methanone (13e). Orange solid. Yield: 60%. m.p 95-96 °C. ^1H NMR (500 MHz, CDCl_3) δ 2.99–3.13 (m, 4H), 3.55 (s, 2H), 3.93 (s, 2H) 5.49 (s, 2H), 5.93 (s, 2H), 6.38 (d, $J=7.5$ Hz, 1H), 6.56 (s, 1H), 6.74 (d, $J=8.5$ Hz, 1H), 7.42 (d, $J=7.0$ Hz, 2H), 7.51 (d, $J=7.5$ Hz, 2H), 8.19 (s, 1H), ^{13}C NMR (125 MHz, CDCl_3): δ 42.9, 47.7, 51.2, 51.6, 54.9, 100.7, 101.0, 108.2, 109.9, 128.2, 128.6, 134.0, 137.4, 142.4, 144.6, 146.7, 148.3, 164.0 169.1. HRMS calcd for $\text{C}_{21}\text{H}_{20}\text{N}_6\text{O}_5$ 436.1495, found $[\text{M} + \text{H}]^+$ 437.1569.

4-((1H-tetrazol-1-yl)methyl)phenyl)(4-(benzo[d][1,3]dioxol-5-yl)piperazin-1-yl)methanone (13f). Off white solid. Yield: 76%. mp 95-95 °C. ^1H NMR (500 MHz, $\text{DMSO}-d_6$): δ 3.04-3.13 (m, 4H), 3.42-3.74 (m, 4H), 5.82 (s, 2H), 5.89 (s, 2H), 6.10 (s, 1H), 6.40 (s, 1H), 6.67

(s, 1H), 7.35-7.49 (m, 4H), 9.00 (s, 1H). ^{13}C NMR (125 MHz, DMSO- d_6): δ 45.2, 47.7, 51.3, 54.6, 70.1, 100.8, 103.0, 108.7, 109.9, 129.0, 136.0, 136.4, 142.4, 143.2, 146.8, 148.3, 152.4, 169.5. HRMS calcd for $\text{C}_{20}\text{H}_{20}\text{N}_6\text{O}_3$ 392.1597, found $[\text{M} + \text{H}]^+$ 393.1668.

(4-(Benzo[d][1,3]dioxol-5-yl)piperazin-1-yl)(4-((3-(hydroxymethyl)-1H-indol-1-yl)methyl)phenyl)methanone (**13g**). To a stirred solution of indole-3-carbinole (1eq) in dry DMF, NaH (1.3 eq, 60%) was added at 0 °C. After 5 min, solid compound **12** (1.2 eq.) was added in one portion and the reaction mixture was stirred at the same temperature for 30 min. Progress of the reaction was monitored with thin layer chromatography. After the completion of the reaction, cold water was added, and the compound was extracted with ethyl acetate (3×15 mL). The combined organic layer was dried over anhydrous sodium sulphate and concentrated under reduce pressure to the the crude mass which was purified with column chromatography using silica gel as a stationary phase and 2% MeOH: CH_2Cl_2 mixture as a mobile phase. Off white solid. Yield: 78%. m.p 151-153 °C. ^1H NMR (500 MHz, DMSO- d_6) δ 2.95-3.03 (m, 4H), 3.33-3.41 (m, 2H), 3.70 (s, 2H), 4.66 (d, $J=5.5$ Hz, 2H), 4.82 (t, $J=5.5$ Hz, 1H), 5.43 (s, 2H), 5.91 (s, 2H), 6.34 (dd, $J_{12}=2.5$ Hz, $J_{13}=8.5$ Hz, 1H), 6.67-6.68 (m, 1H), 6.76 (d, $J=8.5$ Hz, 1H), 7.03 (t, $J=7.0$ Hz, 1H), 7.12 (t, $J=7.0$ Hz, 1H), 7.26 (d, $J=8.5$ Hz, 2H), 7.37 (t, $J=8.5$ Hz, 2H), 7.42 (s, 1H), 7.45 (d, $J=8.5$ Hz, 1H), 7.63 (d, $J=7.5$ Hz, 1H). ^{13}C NMR (125 MHz, DMSO- d_6), δ 49.0, 50.5, 55.7, 65.3, 100.2, 101.0, 108.5, 109.0, 110.4, 116.5, 119.2, 119.7, 121.8, 127.4, 127.5, 127.6, 127.7, 135.2, 136.6, 140.4, 141.4, 147.2, 148.3, 169.1. HRMS calcd for $\text{C}_{28}\text{H}_{27}\text{N}_3\text{O}_4$ 469.2002, found $[\text{M} - \text{OH}]$ 452.1964.

(4-(Benzo[d][1,3]dioxol-5-yl)piperazin-1-yl)(4-(selenocyanatomethyl) phenyl)methanone (**13h**). To a stirred solution of compound **12** (1.0 eq) in acetonitrile, KSeCN (2eq) was added and the reaction mixture was refluxed for 16h. Progress of the reaction was monitored by thin layer chromatography (TLC). Aster the consumption of the starting material, water was added, and the compound was extracted with ethyl acetate. The combined organic fractions were dried over anhydrous sodium sulphate and concentrated to get the crude mass which was purified by flash column chromatography using silica gel and 1% MeOH: CH_2Cl_2 mixture as a eluent to get the pure compound: Off white solid. Yield: 58%. mp 122-124 °C, ^1H NMR (500 MHz, CDCl_3), 3.02-3.13 (m, 4H), 3.56 (s, 2H), 3.94 (s, 2H), 4.32 (s, 2H), 5.93 (s, 2H) 6.39 (dd, $J_{1,2}=2.0$ Hz, $J_{1,3}=8.5$ Hz,

1H), 6.57 (d, $J=2.5$ Hz, 1H), 6.75 (d, $J=8.5$ Hz, 1H), 7.44-7.48(m, 4H). ^{13}C NMR (125 MHz, CDCl_3): δ 32.0, 42.3, 47.8, 51.6, 100.6, 101.0, 101.4, 108.2, 109.8, 128.0, 129.2, 135.9, 137.4, 142.3, 146.8, 148.3, 169.5. HRMS calcd for $\text{C}_{20}\text{H}_{19}\text{N}_3\text{O}_3\text{Se}$ 429.0592, found $[\text{M} + \text{H}]^+$ 430.0667.

1-(4-(4-(Benzo[d][1,3]dioxol-5-yl)piperazine-1-carbonyl)benzyl)thiourea (13i). Off white solid, Yield: 77%. mp 212-215 °C ^1H NMR (500 MHz, $\text{MeOH-}d_4$) δ 3.02-3.14 (m, 4H), 3.58 (s, 2H), 3.91 (s, 2H), 4.52 (s, 2H), 5.89 (s, 2H), 6.45 (dd, $J_{1,2}=2.0$ Hz, $J_{1,3}=8.0$ Hz, 1H), 6.66 (d, $J=2.0$ Hz, 1H), 6.72 (d, $J=8.5$ Hz, 1H), 7.50 (d, $J=8.5$ Hz, 2H), 7.57 (d, $J=8.0$ Hz, 2H). ^{13}C NMR(125MHz, MeOD_4): δ 34.4, 42.1, 50.8, 51.3, 100.3, 100.8, 107.6, 109.6, 127.4, 129.0, 135.4, 136.2, 142.4, 146.9, 148.3, 170.3, 170.4. HRMS calcd for $\text{C}_{20}\text{H}_{22}\text{N}_4\text{O}_3\text{S}$ 398.1413, found $[\text{M} + \text{H}]^+$ 399.1486.

4.1.4. General procedure for the synthesis of compounds **18a-i**

Compounds **18a-i** were synthesized following procedure mentioned for the synthesis of **7a-i**

(4-(Morpholinomethyl)phenyl)(4-(p-tolyl) piperazin-1-yl)methanone (18a). Off white solid. Yield: 70%. mp 135-137 °C. ^1H NMR (500 MHz, CDCl_3): δ 2.30 (s, 3H), 2.49 (s, 4H), 3.10-3.21 (m, 4H), 3.56 (s, 2H), 3.61 (s, 2H), 3.74 (t, $J=4$ Hz, 4H), 3.95 (s, 2H), 6.87 (d, $J=8.5$ Hz, 2H), 7.11(d, $J=8.0$ Hz, 2H), 7.42 (s, 4H). ^{13}C NMR (125 MHz, CDCl_3): δ 20.4, 53.6, 63.3, 66.9, 117.1, 127.2, 129.2, 129.8, 130.3, 134.5, 148.8, 170.3. HRMS calcd for $\text{C}_{23}\text{H}_{29}\text{N}_3\text{O}_2$ 379.5040; found $[\text{M} + \text{H}]^+$ 380.2332.

(4-(Pyrrolidin-1-ylmethyl)phenyl)(4-(p-tolyl)piperazin-1-yl)methanone (18b). Off white solid. Yield: 65%. mp 102-105 °C. ^1H NMR (500 MHz, CDCl_3): δ 1.82 (s, 4H), 2.30 (s, 3H), 2.58 (s, 4H), 3.09-3.21 (m, 4H), 3.63 (m, 6H), 6.87 (d, $J=8.5$ Hz, 2H), 7.11 (d, $J=8.0$ Hz, 2H), 7.41 (s, 4H). ^{13}C NMR (125 MHz, CDCl_3): 20.4, 23.8, 42.2, 47.7, 50.2, 54.2, 60.3, 117.1, 127.2, 128.9, 129.7, 130.2, 134.2, 141.2, 148.8, 170.4. HRMS calcd for $\text{C}_{23}\text{H}_{29}\text{N}_3\text{O}$ 363.2311; found $[\text{M} + \text{H}]^+$ 364.2383.

(4-((1H-Imidazol-1-yl) methyl)phenyl)(4-(p-tolyl)piperazin-1-yl)methanone (18c). Off white solid. Yield: 82%. mp 192-195 °C. ^1H NMR (500 MHz, $\text{DMSO-}d_6$): δ 2.20 (s, 3H), 3.05-3.11 (m, 4H), 3.43-3.71 (m, 4H), 5.47 (s, 2H), 6.81 (d, $J=8.5$ Hz, 2H), 6.94 (s, 1H), 7.03 (d, $J=8.5$ Hz, 2H),

7.15 (s, 1H), 7.34 (d, $J=8.0$ Hz, 2H), 7.47 (d, $J=8.5$ Hz, 2H), 7.62 (s, 1H). ^{13}C NMR(125MHz, DMSO- d_6):

δ 20.3, 41.7, 47.5, 49.3, 52.3, 116.5, 127.7, 128.4, 128.5, 129.7, 135.4, 138.2, 144.3, 149.3, 148.3, 152.4, 169.0. HRMS calcd for $\text{C}_{22}\text{H}_{24}\text{N}_4\text{O}$ 360.1950, found $[\text{M} + \text{H}]^+$ 361.2021.

(4-((1H-1,2,4-Triazol-1-yl)methyl)phenyl)(4-(p-tolyl)piperazin-1-yl)methanone (18d). Off white solid. Yield: 72%. mp 150-152 °C. ^1H NMR (500 MHz, DMSO- d_6): δ 2.20 (s, 3H), 3.04-3.12 (m, 4H), 3.41-3.74 (m, 4H), 5.48 (s, 2H), 6.85 (d, $J=8.5$ Hz, 2H), 7.04 (d, $J=8.5$ Hz, 2H), 7.34 (d, $J=8.0$ Hz, 2H), 7.43 (d, $J=8.5$ Hz, 2H), 8.01 (s, 1H) 8.70 (s, 1H). ^{13}C NMR(125MHz, DMSO- d_6): δ 20.5, 41.9, 47.4, 49.4, 52.1, 116.7, 127.8, 128.2, 128.8, 129.9, 135.8, 138.1, 144.8, 149.1, 152.3, 169.0. HRMS calcd for $\text{C}_{21}\text{H}_{23}\text{N}_5\text{O}$ 361.1903, found $[\text{M} + \text{H}]^+$ 362.1977.

(4-((3-Nitro-1H-1,2,4-triazol-1-yl)methyl)phenyl)(4-(p-tolyl)piperazin-1-yl)methanone(18e). Yellow solid. Yield: 62%. mp 75-78 °C. ^1H NMR (500 MHz, CDCl_3): δ 2.30 (s, 3H), 3.08-3.22 (m, 4H), 3.57-3.95 (m, 4H), 5.49 (s, 2H), 6.86 (d, $J=8.0$ Hz, 2H), 7.11 (d, $J=8.0$ Hz, 2H), 7.42 (d, $J=8.0$ Hz, 2H), 7.51 (d, $J=7.5$ Hz, 2H), 8.20 (s, 1H). ^{13}C NMR(125MHz, CDCl_3): δ 20.4, 42.3, 50.1, 50.5, 54.8, 117.1, 128.2, 128.6, 129.8, 134.1, 137.0, 144.7, 148.7, 169.1. HRMS calcd for $\text{C}_{21}\text{H}_{22}\text{N}_6\text{O}_3$ 406.4460, found $[\text{M} + \text{H}]^+$ 404.1828.

(4-((1H-Tetrazol-1-yl) methyl)phenyl)(4-(p-tolyl)piperazin-1-yl)methanone (18f). Off white solid. Yield: 74%. mp 136-138 °C. ^1H NMR (500 MHz, DMSO- d_6): δ 2.20 (s, 3H), 3.04-3.13 (m, 4H), 3.42-3.74 (m, 4H), 6.03 (s, 2H), 6.85 (d, $J=8.5$ Hz, 2H), 7.04 (d, $J=8.5$ Hz, 2H), 7.42-7.47 (m,4H), 9.02 (s, 1H). ^{13}C NMR (125 MHz, DMSO- d_6): δ 20.5, 41.9, 47.4, 49.4, 55.8,116.7, 128.0, 128.8, 129.9, 135.8, 136.4, 149.1, 154.1, 168.9. HRM S calcd for $\text{C}_{20}\text{H}_{22}\text{N}_6\text{O}$ 362.1855, found $[\text{M} + \text{H}]^+$ 363.1934.

(4-((3-(Hydroxymethyl)-1H-indol-1-yl) methyl) phenyl)(4-(p-tolyl)piperazin-1-yl)methanone (18g). Off white solid. Yield: 68%. mp 76-78 °C. ^1H NMR (500 MHz, DMSO- d_6):2.61 (s, 4H), 3.00-3.14 (m, 8H), 3.56 (s, 2H), 3.93 (s, 2H), 4.21 (s, 2H), 5.93 (s, 2H), 6.38 (d, $J=7.0$ Hz, 1H), 6.57 (s, 1H), 6.74 (d, $J=8.5$ Hz, 2H), 7.52 (d, $J=8.0$ Hz, 2H), 7.75 (d, $J=8.0$ Hz, 2H). ^{13}C NMR (125MHz,

CDCl₃): δ 23.1, 42.3, 47.7, 51.2, 53.3, 58.2, 100.7, 101.0, 108.2, 109.9, 128.1, 130.6, 137.0, 142.3, 146.8, 148.3, 169.3. HRMS calcd for C₂₈H₂₉N₃O₂ 439.2260, found [M –OH] 422.2226.

(4-(Selenocyanatomethyl) phenyl)(4-(*p*-tolyl)piperazin-1-yl)methanone (**18h**). Off white solid. Yield: 52%. mp 161-162 °C. ¹H NMR (500 MHz, CDCl₃): δ 2.21 (s, 3H), 3.10 (br s, 4H), 3.47-3.75 (m, 4H), 4.35 (s, 2H), 6.86 (d, *J*=8.0 Hz, 2H), 7.04 (d, *J*=8.5 Hz, 2H), 7.43-7.47 (m, 4H). ¹³C NMR (125MHz, CDCl₃): δ 20.5, 32.5, 41.9, 47.4, 49.5, 105.4,116.7, 127.8, 128.7, 129.3, 129.9, 136.6, 140.4, 149.1, 169.1. HRMS calcd for C₂₀H₂₁N₃OSe 399.0850, found [M + H]⁺ 400.0923.

1-(4-(4-(*p*-Tolyl)piperazine-1-carbonyl)benzyl) thiourea (**18i**). Off white solid. Yield: 75%. mp 209-211 °C. ¹H NMR (500 MHz, DMSO-d₆): δ 2.20 (s, 3H), 3.07-3.12 (m, 4H), 3.47-3.754 (m, 4H), 4.55 (s, 2H), 6.86 (d, *J*=8.0 Hz, 2H), 7.04 (d, *J*=8.5 Hz, 2H), 7.45 (d, *J*=8.0 Hz, 2H), 7.51 (d, *J*=8.0 Hz, 2H), 9.18 (br s, 3H). ¹³C NMR (125MHz, CDCl₃): δ 20.3, 32.5, 41.9, 47.4, 49.5,116.7, 120.0, 128.8, 129.4, 129.9, 135.8, 137.1, 149.1, 169.0, 169.3. HRMS calcd for C₂₀H₂₄N₄OS 368.1671; found [M + H]⁺ 369.1748.

4.2. Biology

4.2.1. Split-luciferase assay

We have previously reported the generation and validation of our split luciferase assay.[30] Briefly, RKO cells were seeded in DMEM with 10% calf serum, 24 hrs prior to the transfection. Transfection was done using Lipofectamine 2000 with reporter plasmids and Renilla-luciferase expressing vector (as internal control). After 24 hrs, cells were lysed, and clear lysates were used for luciferase assay. To test the effects of all analogs of compound 7773, transfected cells with reporter plasmids were washed with PBS after 24 hrs of transfection and incubated with medium containing 7773 or its analogs.

4.2.2. Cloning, expression, and purification of recombinant proteins

Human IGF2BP11 (hIGF2BP1) di-domains KH12 (V194-N369) and KH34 (P387-A574) cDNA sequences were cloned in pETM30 and pETM11 bacterial expression vectors (EMBL) respectively, as previously reported.[30, 36] The ¹⁵N-labelled N-6xHis-KH34 and N-6xHis/GST-

KH12 fusion proteins were expressed in *E. coli* BL21(DE3) (Invitrogen), by culturing the cells in M9 minimal medium[37] supplemented with 1 g/L of $^{15}\text{NH}_4\text{Cl}$ and 6 g/L of D-glucose as sole sources of nitrogen and carbon. Cells were grown at 37°C up to exponential phase and expression induced by adding 0.5 mM Isopropyl β -d-1-thiogalactopyranoside and culturing the cells overnight at 18°C. After cell lysis and sonication in 10 mM TRIS-Base pH 8.0, 10 mM imidazole, 1 M NaCl, 5% glycerol, 2 mM 2-Mercaptoethanol, a tablet of cOmplete™ protease inhibitor cocktail (Roche) per 50 mL of buffer, 0.01 % Triton-X (Sigma), 200 $\mu\text{g}/\text{mL}$ lysozyme (Sigma), the proteins were purified by immobilised metal affinity chromatography (IMAC). Tags were removed by overnight cleavage with 5 μM TEV protease at 4°C in 50 mM TRIS-Base pH 7.5, 150 mM NaCl, 2 mM 2-Mercaptoethanol. RNA contaminants were removed by cation-exchange in Hi-Load SP-Sepharose 26/10 column (GE Healthcare), eluting with a 0-100% gradient of 10 mM TRIS-Base, 1 M NaCl, 2 mM 2-Mercaptoethanol. The sample were size-excluded in Hi-Load 16/600 Superdex 75 pg (GE Healthcare), equilibrated with 10 mM Na_2HPO_4 pH 7.4, 50 mM NaCl, 1 mM tris(2-carboxyethyl)phosphine) (TCEP). The purity of the purified proteins was assessed using SDS gel electrophoresis,[38] while protein concentration was measured using the sample absorbance at 280 nm.[39] Samples were snap frozen in small aliquots and stored at -80 °C for use in further experiments.

4.2.3. Nuclear Magnetic Resonance (NMR) titrations

NMR titrations experiments were recorded at 25°C on a Bruker Avance spectrometer operating at 800 MHz ^1H frequency. Heteronuclear single quantum coherence (^{15}N -HSQC) experiments [40] were performed by adding the AVJ16 compound (0.1 M DMSO stock) into samples of ^{15}N -KH12 and ^{15}N -KH34, obtaining protein-to-AVJ16 molar ratios of 1:0.25, 0.5, 0.75, 1, 1.5, 2, 3, 4, 6, 8, 11, 14, in 10 mM Na_2HPO_4 pH 7.4, 50 mM NaCl, 1 mM (TCEP), 10% D_2O , 0.02% NaN_3 . All NMR spectra were processed using NMRpipe [41] and analysed with CCPN [42] and TopSpin 4.0.6 (Bruker) software. Chemical shifts perturbations (CSP) were calculated using the formula:

$$\text{CSP} = \sqrt{(\delta_{^1\text{H}})^2 + 0.15 (\delta_{^{15}\text{N}})^2}$$

where δ_{1H} and δ_{15N} are the chemical shift differences of the 1H and ^{15}N dimensions, respectively. The published ^{15}N -HSQC resonance assignments [24, 36] were obtained from the Biological Magnetic Resonance Bank database and transferred to our ^{15}N -HSQC spectra.

4.2.4. Cell lines and cell culture

The CRC cell lines, RKO and HCT116 were cultured in Dulbecco's modified Eagle medium (DMEM; Corning) and McCoy's 5A medium (McCoy's: Corning) respectively, supplemented with 10% fetal bovine serum (FBS; Gibco). The CRC cell lines SW480 (SW480-WT) and SW480-IGF2BP1-knockout (SW480-IGF2BP1-KO) were the generous gift from Dr. Kathryn E Hamilton,[43] and these cell lines were cultured in DMEM supplemented with 10% FBS. All the CRC cell lines were maintained at 37°C, 5% CO₂.

4.2.5. Cell proliferation assay

The IncuCyte, a real-time imaging system, was used to measure cell proliferation using a label-free cell monolayer confluence approach. IncuCyte acquires high-quality, phase-contrast images and uses an integrated confluence metric as a surrogate for cell number. We determined the effect of compound **13g** on the proliferation of RKO and HCT116 CRC cell lines by comparing the confluence between **13g** treated and DMSO (vehicle control) treated cells. Images were captured every 4 h for 96 h from three separate regions per well using a 10× objective. The green object count per region was quantified at each time point. IncuCyte data were analyzed by one-way analysis of variance (ANOVA) with Tukey's multiple comparison test using GraphPad Prism software. The results were shown as mean \pm standard deviation (SD) for three independent experiments. *p* values of < 0.05 were considered to be significant.

4.2.6. IncuCyte apoptosis assay

To determine the effect of **13g** on CRC cells, we utilized the Caspase-3/7 apoptosis assay and monitored the experiment by IncuCyte live cell imaging system. Briefly, RKO and HCT116 cells were seeded at 5000 cells per well in a 96-well plate (Corning). After incubating overnight, compound **13g** and the Caspase-3/7 reagent (Sartorius) were added. The analysis was done as described in the above paragraph.

4.2.7. Scratch wounding migration assay

The IncuCyte system was used for scratch wounding migration assay. SW480-WT and SW480-IGF2BP1-KO cells were grown in 96-well culture plates. Cell layers were scraped with a pin block and then incubated at 37°C. Pictures were taken at set time points by IncuCyte system. The Incucyte image analysis software was used to detect cell edges and generate an overlay mask, which was used to calculate the cell coverage area. Images were captured every 4 h for 72 h from two separate regions per well using a 10× objective. The results were shown as mean ± standard error (SE) for three independent experiments. *P* values of < 0.05 were considered to be significant.

4.2.8. Microscale thermophoresis (MST)

MST analysis was performed as described [Wallis et al., 2022]. In short, recombinant full-length Igf2bp1 protein was labelled with RED-tris-NTA dye using a Monolith NT His-Tag Labelling Kit (NanoTemper) and the di-domain peptides were labelled using the Protein Labeling Kit RED NHS 2nd generation (NanoTemper). Labelled proteins were spun at 15,000g for 5 min to eliminate aggregates and were combined with serial dilutions of either compound or target Kras6 RNA at room temperature for 15 min. Samples were then loaded into standard capillaries and processed. Results were analyzed using the MO Control software (NanoTemper) for curve fitting to K_D .

Author Contributions

The manuscript was written through contributions of all authors. All authors have given approval to the final version of the manuscript.

Declaration of competing interest

The authors declare no competing financial interests or personal relationships that could inappropriately influence the reported work.

Acknowledgements

AKS and VSS thank the Department of Pharmacology, Penn State College of Medicine (PSCOM), Penn State Cancer Institute (PSCI), Pediatrics Department at PSCOM, and Four Diamonds Fund

Research Program for financial support. The authors thank the Organic Synthesis Shared Resource, Flow Cytometry Shared Resource and Solution Phase NMR Facility (Dr. Jyh-Ming Lin) at Core Research Facilities of the PSCI and PSCOM. We also thanks to Penn State Metabolomics Facility - University Park, PA for HRMS calculation. JKY was funded by grants from the Israel Cancer Research Foundation, the Israel Science Foundation, and Integra Holdings Ltd.

Supplementary data. Copies of the ^1H NMR and ^{13}C NMR spectra for new compounds **7a-h**, **13g-i** and **18g-I**, Figure 1S and Figure 2S.

Abbreviations

HSQC	Heteronuclear single quantum coherence
I3C	Indole-3-carbinol
IGF2BP1	Insulin like growth factor 2 mRNA binding protein 1
MST	Microscale thermophoresis
mRNA	Messenger ribonucleic acid
N-boc	N-tert-butyloxycarbonyl
NMR	Nuclear magnetic resonance
RNA	Ribonucleic acid

REFERENCES

- [1] N. Degrauwe, M.L. Suva, M. Janiszewska, N. Riggi, I. Stamenkovic, IMPs: an RNA-binding protein family that provides a link between stem cell maintenance in normal development and cancer, *Genes Dev*, 30 (2016) 2459-2474.

- [2] T.V. Hansen, N.A. Hammer, J. Nielsen, M. Madsen, C. Dalbaeck, U.M. Wewer, J. Christiansen, F.C. Nielsen, Dwarfism and impaired gut development in insulin-like growth factor II mRNA-binding protein 1-deficient mice, *Mol Cell Biol*, 24 (2004) 4448-4464.
- [3] J. Ross, I. Lemm, B. Berberet, Overexpression of an mRNA-binding protein in human colorectal cancer, *Oncogene*, 20 (2001) 6544-6550.
- [4] C.R. Tessier, G.A. Doyle, B.A. Clark, H.C. Pitot, J. Ross, Mammary tumor induction in transgenic mice expressing an RNA-binding protein, *Cancer Res*, 64 (2004) 209-214.
- [5] I. Elcheva, R.S. Tarapore, N. Bhatia, V.S. Spiegelman, Overexpression of mRNA-binding protein CRD-BP in malignant melanomas, *Oncogene*, 27 (2008) 5069-5074.
- [6] T. Kato, S. Hayama, T. Yamabuki, N. Ishikawa, M. Miyamoto, T. Ito, E. Tsuchiya, S. Kondo, Y. Nakamura, Y. Daigo, Increased expression of insulin-like growth factor-II messenger RNA-binding protein 1 is associated with tumor progression in patients with lung cancer, *Clin Cancer Res*, 13 (2007) 434-442.
- [7] J.L. Bell, R. Turlapati, T. Liu, J.H. Schulte, S. Huttelmaier, IGF2BP1 harbors prognostic significance by gene gain and diverse expression in neuroblastoma, *J Clin Oncol*, 33 (2015) 1285-1293.
- [8] I. Elcheva, S. Goswami, F.K. Noubissi, V.S. Spiegelman, CRD-BP protects the coding region of betaTrCP1 mRNA from miR-183-mediated degradation, *Mol Cell*, 35 (2009) 240-246.
- [9] S. Goswami, R.S. Tarapore, A.M. Poenitzsch Strong, J.J. TeSlaa, Y. Grinblat, V. Setaluri, V.S. Spiegelman, MicroRNA-340-mediated degradation of microphthalmia-associated transcription factor (MITF) mRNA is inhibited by coding region determinant-binding protein (CRD-BP), *J Biol Chem*, 290 (2015) 384-395.
- [10] F.K. Noubissi, I. Elcheva, N. Bhatia, A. Shakoori, A. Ougolkov, J. Liu, T. Minamoto, J. Ross, S.Y. Fuchs, V.S. Spiegelman, CRD-BP mediates stabilization of betaTrCP1 and c-myc mRNA in response to beta-catenin signalling, *Nature*, 441 (2006) 898-901.
- [11] F.K. Noubissi, S. Goswami, N.A. Sanek, K. Kawakami, T. Minamoto, A. Moser, Y. Grinblat, V.S. Spiegelman, Wnt signaling stimulates transcriptional outcome of the Hedgehog pathway by stabilizing GLI1 mRNA, *Cancer Res*, 69 (2009) 8572-8578.
- [12] P.S. Mongroo, F.K. Noubissi, M. Cuatrecasas, J. Kalabis, C.E. King, C.N. Johnstone, M.J. Bowser, A. Castells, V.S. Spiegelman, A.K. Rustgi, IMP-1 displays cross-talk with K-Ras

- and modulates colon cancer cell survival through the novel proapoptotic protein CYFIP2, *Cancer Res*, 71 (2011) 2172-2182.
- [13] X. Huang, H. Zhang, X. Guo, Z. Zhu, H. Cai, X. Kong, Insulin-like growth factor 2 mRNA-binding protein 1 (IGF2BP1) in cancer, *J Hematol Oncol*, 11 (2018) 88.
- [14] E.A. Craig, V.S. Spiegelman, Inhibition of coding region determinant binding protein sensitizes melanoma cells to chemotherapeutic agents, *Pigment Cell Melanoma Res*, 25 (2012) 83-87.
- [15] T. Kim, T. Havighurst, K. Kim, M. Albertini, Y.G. Xu, V.S. Spiegelman, Targeting insulin-like growth factor 2 mRNA-binding protein 1 (IGF2BP1) in metastatic melanoma to increase efficacy of BRAF(V600E) inhibitors, *Mol Carcinog*, 57 (2018) 678-683.
- [16] J.M. Biegel, M. Dhamdhere, S. Gao, C.P. Gowda, Y.I. Kawasawa, V.S. Spiegelman, Inhibition of the mRNA-Binding Protein IGF2BP1 Suppresses Proliferation and Sensitizes Neuroblastoma Cells to Chemotherapeutic Agents, *Front Oncol*, 11 (2021) 608816.
- [17] I.A. Elcheva, T. Wood, K. Chiarolanzio, B. Chim, M. Wong, V. Singh, C.P. Gowda, Q. Lu, M. Hafner, S. Dovat, Z. Liu, S.A. Muljo, V.S. Spiegelman, RNA-binding protein IGF2BP1 maintains leukemia stem cell properties by regulating HOXB4, MYB, and ALDH1A1, *Leukemia*, 34 (2020) 1354-1363.
- [18] N. Betson, M. Hajahmed, T. Gebretsadek, K. Ndebele, H.A. Ahmad, P.B. Tchounwou, V.S. Spiegelman, F.K. Noubissi, Inhibition of insulin-like growth factor 2 mRNA-binding protein 1 sensitizes colorectal cancer cells to chemotherapeutics, *FASEB Bioadv*, 4 (2022) 816-829.
- [19] K.E. Hamilton, F.K. Noubissi, P.S. Katti, C.M. Hahn, S.R. Davey, E.T. Lundsmith, A.J. Klein-Szanto, A.D. Rhim, V.S. Spiegelman, A.K. Rustgi, IMP1 promotes tumor growth, dissemination and a tumor-initiating cell phenotype in colorectal cancer cell xenografts, *Carcinogenesis*, 34 (2013) 2647-2654.
- [20] A. Ghoshal, L.C. Rodrigues, C.P. Gowda, I.A. Elcheva, Z. Liu, T. Abraham, V.S. Spiegelman, Extracellular vesicle-dependent effect of RNA-binding protein IGF2BP1 on melanoma metastasis, *Oncogene*, 38 (2019) 4182-4196.
- [21] M.R. Dhamdhere, C.P. Gowda, V. Singh, Z. Liu, N. Carruthers, C.N. Grant, A. Sharma, S. Dovat, J.M. Sundstrom, H.G. Wang, V.S. Spiegelman, IGF2BP1 regulates the cargo of extracellular vesicles and promotes neuroblastoma metastasis, *Oncogene*, (2023).

- [22] Y. Xi, Y. Wang, IGF2BP1, a New Target to Overcome Drug Resistance in Melanoma?, *Front Pharmacol*, 13 (2022) 947363.
- [23] T.Y. Zhu, L.L. Hong, Z.Q. Ling, Oncofetal protein IGF2BPs in human cancer: functions, mechanisms and therapeutic potential, *Biomark Res*, 11 (2023) 62.
- [24] V.L. Patel, S. Mitra, R. Harris, A.R. Buxbaum, T. Lionnet, M. Brenowitz, M. Girvin, M. Levy, S.C. Almo, R.H. Singer, J.A. Chao, Spatial arrangement of an RNA zipcode identifies mRNAs under post-transcriptional control, *Genes Dev*, 26 (2012) 43-53.
- [25] J. Vikesaa, T.V. Hansen, L. Jonson, R. Borup, U.M. Wewer, J. Christiansen, F.C. Nielsen, RNA-binding IMPs promote cell adhesion and invadopodia formation, *EMBO J*, 25 (2006) 1456-1468.
- [26] F.C. Nielsen, J. Nielsen, M.A. Kristensen, G. Koch, J. Christiansen, Cytoplasmic trafficking of IGF-II mRNA-binding protein by conserved KH domains, *J Cell Sci*, 115 (2002) 2087-2097.
- [27] G. Nicastro, G. Abis, P. Klein, S. Esteban-Serna, C. Gallagher, B. Chaves-Arquero, Y. Cai, A.M. Figueiredo, S.R. Martin, R. Patani, I.A. Taylor, A. Ramos, Direct m6A recognition by IMP1 underlies an alternative model of target selection for non-canonical methyl-readers, *Nucleic Acids Res*, 51 (2023) 8774-8786.
- [28] H. Huang, H. Weng, W. Sun, X. Qin, H. Shi, H. Wu, B.S. Zhao, A. Mesquita, C. Liu, C.L. Yuan, Y.C. Hu, S. Huttelmaier, J.R. Skibbe, R. Su, X. Deng, L. Dong, M. Sun, C. Li, S. Nachtergaele, Y. Wang, C. Hu, K. Ferchen, K.D. Greis, X. Jiang, M. Wei, L. Qu, J.L. Guan, C. He, J. Yang, J. Chen, Recognition of RNA N(6)-methyladenosine by IGF2BP proteins enhances mRNA stability and translation, *Nat Cell Biol*, 20 (2018) 285-295.
- [29] J.P. Falese, A. Donlic, A.E. Hargrove, Targeting RNA with small molecules: from fundamental principles towards the clinic, *Chem Soc Rev*, 50 (2021) 2224-2243.
- [30] N. Wallis, F. Oberman, K. Shurrush, N. Germain, G. Greenwald, T. Gershon, T. Pearl, G. Abis, V. Singh, A. Singh, A.K. Sharma, H.M. Barr, A. Ramos, V.S. Spiegelman, J.K. Yisraeli, Small molecule inhibitor of Igf2bp1 represses Kras and a pro-oncogenic phenotype in cancer cells, *RNA Biol*, 19 (2022) 26-43.
- [31] J.R. Weng, C.H. Tsai, S.K. Kulp, C.S. Chen, Indole-3-carbinol as a chemopreventive and anti-cancer agent, *Cancer Lett*, 262 (2008) 153-163.

- [32] C. Sherer, I. Tolaymat, F. Rowther, T. Warr, T.J. Snape, Preliminary SAR on indole-3-carbinol and related fragments reveals a novel anticancer lead compound against resistant glioblastoma cells, *Bioorg Med Chem Lett*, 27 (2017) 1561-1565.
- [33] R. Dagil, N.J. Ball, R.W. Ogradowicz, F. Hobor, A.G. Purkiss, G. Kelly, S.R. Martin, I.A. Taylor, A. Ramos, IMP1 KH1 and KH2 domains create a structural platform with unique RNA recognition and re-modelling properties, *Nucleic Acids Res*, (2019).
- [34] Y.B. Rosenfeld, M. Krumbein, A. Yeffet, N. Schiffmann, I. Mishalian, E. Pikarsky, F. Oberman, Z. Fridlender, J.K. Yisraeli, VICKZ1 enhances tumor progression and metastasis in lung adenocarcinomas in mice, *Oncogene*, 38 (2019) 4169-4181.
- [35] E.A. Craig, J.D. Weber, V.S. Spiegelman, Involvement of the mRNA binding protein CRD-BP in the regulation of metastatic melanoma cell proliferation and invasion by hypoxia, *J Cell Sci*, 125 (2012) 5950-5954.
- [36] R. Dagil, N.J. Ball, R.W. Ogradowicz, F. Hobor, A.G. Purkiss, G. Kelly, S.R. Martin, I.A. Taylor, A. Ramos, IMP1 KH1 and KH2 domains create a structural platform with unique RNA recognition and re-modelling properties, *Nucleic Acids Res*, 47 (2019) 4334-4348.
- [37] L.P. McIntosh, F.W. Dahlquist, Biosynthetic incorporation of ¹⁵N and ¹³C for assignment and interpretation of nuclear magnetic resonance spectra of proteins, *Q Rev Biophys*, 23 (1990) 1-38.
- [38] U.K. Laemmli, Cleavage of structural proteins during the assembly of the head of bacteriophage T4, *Nature*, 227 (1970) 680-685.
- [39] M.R. Wilkins, E. Gasteiger, A. Bairoch, J.C. Sanchez, K.L. Williams, R.D. Appel, D.F. Hochstrasser, Protein identification and analysis tools in the ExPASy server, *Methods Mol Biol*, 112 (1999) 531-552.
- [40] J. Cavanagh, W.J. Fairbrother, A.G. Palmer, M. Rance, N.J. Skelton, CHAPTER 1 - CLASSICAL NMR SPECTROSCOPY, in: J. Cavanagh, W.J. Fairbrother, A.G. Palmer, M. Rance, N.J. Skelton (Eds.) *Protein NMR Spectroscopy (Second Edition)*, Academic Press, Burlington, 2007, pp. 1-28.
- [41] F. Delaglio, S. Grzesiek, G.W. Vuister, G. Zhu, J. Pfeifer, A. Bax, NMRPipe: a multidimensional spectral processing system based on UNIX pipes, *J Biomol NMR*, 6 (1995) 277-293.

- [42] W.F. Vranken, W. Boucher, T.J. Stevens, R.H. Fogh, A. Pajon, M. Llinas, E.L. Ulrich, J.L. Markley, J. Ionides, E.D. Laue, The CCPN data model for NMR spectroscopy: development of a software pipeline, *Proteins*, 59 (2005) 687-696.
- [43] P. Chatterji, P.A. Williams, K.A. Whelan, F.C. Samper, S.F. Andres, L.A. Simon, L.R. Parham, R. Mizuno, E.T. Lundsmith, D.S. Lee, S. Liang, H.S. Wijeratne, S. Marti, L. Chau, V. Giroux, B.J. Wilkins, G.D. Wu, P. Shah, G.G. Tartaglia, K.E. Hamilton, Posttranscriptional regulation of colonic epithelial repair by RNA binding protein IMP1/IGF2BP1, *EMBO Rep*, 20 (2019).